Editors' Suggestion

Chern-textured exciton insulators with valley spiral order in moiré materials

Ziwei Wang,[1,*] Yves H. Kwan,[2,*] Glenn Wagner,[3] Steven H. Simon,[1] Nick Bultinck,[4] and S. A. Parameswaran[1]
[1]*Rudolf Peierls Centre for Theoretical Physics, University of Oxford, Parks Road, Oxford OX1 3PU, United Kingdom*
[2]*Princeton Center for Theoretical Science, Princeton University, Princeton, New Jersey 08544, USA*
[3]*Department of Physics, University of Zurich, Winterthurerstrasse 190, 8057 Zurich, Switzerland*
[4]*Department of Physics, Ghent University, Krijgslaan 281, 9000 Gent, Belgium*

(Received 31 October 2024; revised 2 March 2025; accepted 11 March 2025; published 11 July 2025)

We explore the phase diagrams of moiré materials in search of a class of intervalley-coherent correlated insulating state: the Chern texture insulator (CTI). This phase of matter, proposed in a companion paper [Kwan *et al.*, Phys. Rev. B **112**, 035129 (2025).], breaks valley $U(1)$ symmetry in a nontrivial fashion wherein the valley order parameter is forced to texture in momentum space as a consequence of band topology. Using detailed Hartree-Fock studies, we establish that the CTI emerges as an energetically competitive intermediate-coupling ground state in several moiré systems that lack a twofold rotation symmetry that forbids the single-particle topology essential to the formation of the CTI valley texture.

DOI: 10.1103/chsd-123t

I. INTRODUCTION

Moiré materials—heterostructures of layered atomically-thin constituents stacked with a lattice or rotational mismatch—have ushered in a new paradigm of correlated electronic matter with unprecedented tunability and diversity. Experiments in recent years have uncovered a rich variety of strongly-interacting phenomena including superconductivity [1–4], correlated insulators [2,3,5], orbital ferromagnetism [6,7], (fractional) Chern insulators [8–13], linear-T resistivity [14,15], generalized Wigner crystals [16], and many others. The pioneering studies focused on magic-angle twisted bilayer graphene (TBG), but an ever-growing research effort has been invested into other systems involving larger numbers of layers [17,18] and alternative material building blocks [19]. While different moiré platforms can vary significantly in the details of their single-particle models and hence interacting phenomenology, they often share several fundamental features. Firstly, the region in parameter space of greatest interest is typically where some subset of the bands are isolated and narrow, and electronic interactions can be expected to play a nontrivial role. Secondly, most moiré materials carry flavor degrees of freedom such as spin and valley, which can participate in symmetry-breaking phenomena. Finally, the low-energy moiré bands are often topologically nontrivial.

The confluence of these three features has motivated parallels to an older problem: namely, that of quantum Hall ferromagnetism (QHFM) [20]. This is usually exhibited by electrons with flavor degrees of freedom in exactly-flat bands characterized by a topological Chern number $C = 1$: the celebrated Landau levels of electrons in a magnetic field. A direct analogy between the two problems is complicated by two facts. The first is that single-particle moiré bands intrinsically preserve time-reversal symmetry ($\hat{\mathcal{T}}$), whose breaking is a prerequisite for $C \neq 0$. This means that the bands either (i) do not have a readily definable Chern number (as is the case, for instance, when they are endowed with an additional $\hat{\mathcal{C}}_{2z}$ spatial rotation symmetry, leading to a distinct "Euler invariant" topological index); or else (ii) come in time-reversed partners with equal and opposite Chern numbers. The second is that moiré bands are never exactly flat, and moreover interactions can feed back nontrivially on their dispersion, potentially modifying the balance of interaction and kinetic energy. Together, these open the possibility for new phases of matter unanticipated from the strong-coupling, QHFM-like limit.

Pursuing this line of inquiry, in a companion work [21] we introduced a class of broken-symmetry topological phase that we termed the "textured exciton insulator" (TEI), as a candidate ground state for moiré materials whose single-particle bands are topological and carry a conserved $U(1)_V$ "valley" charge. Here, the excitonic order parameter introduces intervalley coherence, thereby spontaneously breaks $U(1)_V$, and is forced to "texture" across the Brillouin zone because of the mandates of band topology [22]. We established several universal aspects of TEIs linked to their intertwining of symmetry-breaking and topology, including identifying a topological obstruction to giving them a local-moment description [21].

TEIs come in two varieties, depending on the two classes of time-reversal-invariant band structure discussed above. The first, the "Euler texture insulator" (ETI) is linked to $\hat{\mathcal{C}}_{2z}\hat{\mathcal{T}}$-invariant bands with a nonzero Euler index in each valley [23–25], whereas the second, the "Chern texture insulator" emerges in $\hat{\mathcal{C}}_{2z}$-broken systems with valley-contrasting Chern numbers. Using general arguments and simplified toy models, we demonstrated in Ref. [21] that TEIs are energetically

*These authors contributed equally to this work.

Published by the American Physical Society under the terms of the Creative Commons Attribution 4.0 International license. Further distribution of this work must maintain attribution to the author(s) and the published article's title, journal citation, and DOI.

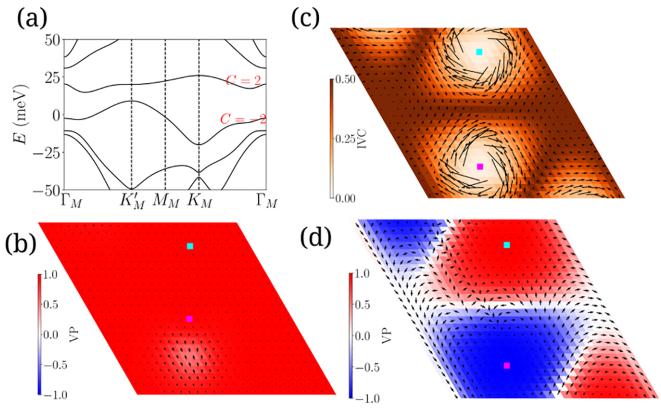


FIG. 1. ABAB-stacked twisted double-bilayer graphene (TDBG) at $\theta = 1.2^\circ$. (a) Single-particle band structure at $\Delta V = 40$ meV in valley K ($\tau = +$). (b) Momentum-dependent valley polarization (VP), shown as color, and intervalley coherence (IVC), shown with arrows, of the $\nu = +2$ tilted valley polarized (TVP) state at $\Delta V = 40$ meV and $\epsilon_r = 17$, from 24×24 HF. Cyan (magenta) square denotes Γ_M point of valley K (K'). We also note that TVP has incommensurate $\boldsymbol{q}$, as the minimum of the noninteracting conduction band is not at a high-symmetry momentum. (c) The IVC intensity, shown as color, and gauge-invariant velocity [Eq. (24)], shown with arrows, of the $\nu = +2$ CTI_2 at $\Delta V = 40$ meV and $\epsilon_r = 20$, from 24×24 HF. Diverging velocities very close to vortex cores are not shown. (d) Same as (b) except for the CTI_2 shown in (c). We observe that the intervalley order winds by 8π around the mBZ, which is consistent with the Chern number difference of 4 between the conduction band in the K and K' valleys. We point out that (c) and (d) have a different $\boldsymbol{q}$ compared to (b), resulting in different relative positions for the Γ_M points in the two valleys. For (b)–(d), we only show the quantities in one spin sector.

competitive ground states at intermediate coupling at some partial (integer) filling of the bands. In the ETI case, we further identified the incommensurate Kekulé spiral (IKS) phase predicted [26], and subsequently observed [27,28] in magic-angle bi/trilayer [29] graphene as an ETI. Given that this establishes the ETI as an experimentally relevant concept, this naturally stimulates a search for its Chern-textured counterpart in other systems.

With this motivation, here we explore the phase diagrams of different moiré materials that break $\hat{\mathcal{C}}_{2z}$ either explicitly or spontaneously. These materials, in the parameter regimes investigated in this paper, have band widths of about ∼10 meV {see theoretical single-band structures in Figs. 1(a), 3(a), 6(b), 8(a), and 10(a), and experimental measurements of the local density-of-states in Refs. [30–32]}, similar to the typical Coulomb interaction energy scale. As such, we expect CTIs, which are natural candidate phases at intermediate-coupling, to be relevant in these materials. Indeed, using microscopically faithful self-consistent Hartree-Fock (HF) calculations, we demonstrate that CTIs are energetically competitive ground states in many of these materials. En route, we address the various further complications of realistic materials absent in simplified models, such as various competing orders, the interaction-induced hybridization of single-particle bands within each valley, etc. Even after incorporating these features, we find that robust CTI order survives within a reasonable parameter regime across a large class of materials, as summarized in Table I. In each of these cases, the order is linked to a moiré-scale modulation of intervalley coherence, that in several cases can potentially be directly detected through scanning probe measurements similar to those used to identify IKS order [27,28]. Our work thus provides yet another illustration of how the combinatorial versatility of moiré systems provides fertile ground for seeking new and complex correlated states of matter with cutting-edge probes.

The remainder of this paper is organized as follows. In Sec. II, we briefly summarize the theory of the CTI, summarize the single-particle continuum models of the moiré materials considered in this paper, and discuss details of the HF calculations. We present the results of our numerical stud-

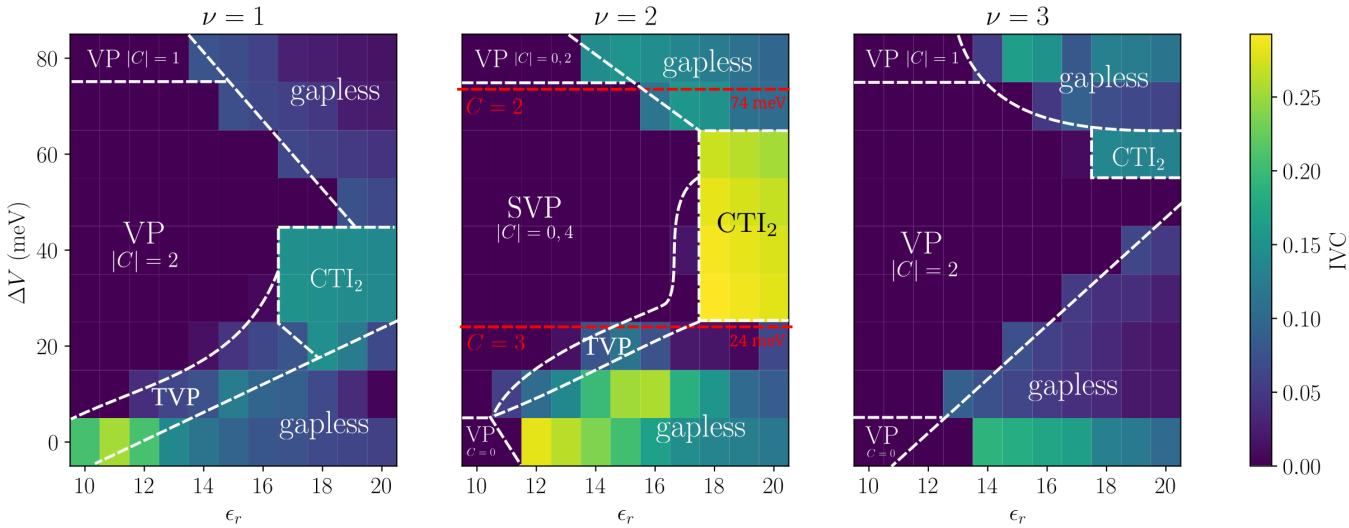


FIG. 2. Phase diagram of ABAB-stacked twisted double-bilayer graphene (TDBG) at $\theta = 1.2^\circ$. The results are obtained using 12×12 HF at $\nu = 1, 2, 3$. VP denotes valley-polarized states, which also carry a nonzero spin polarization. SVP denotes spin- or valley-polarized states, which are degenerate in HF. TVP denotes tilted valley-polarized states. Topological transitions in the noninteracting band structure are marked in red, with the Chern number labels that of the central conduction band.

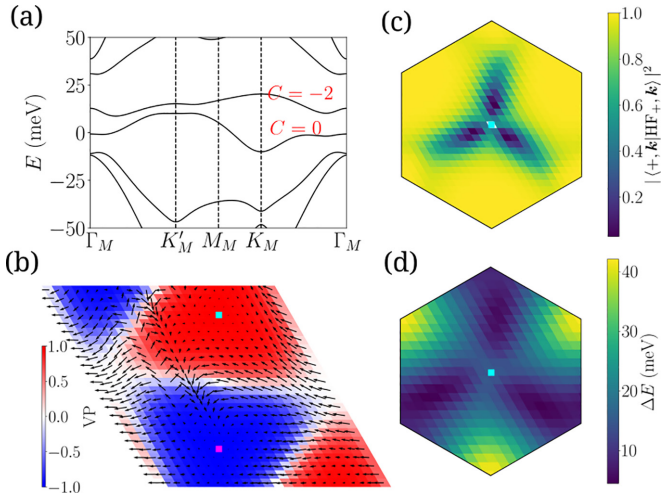


FIG. 3. ABBA-stacked twisted double-bilayer graphene (TDBG) at $\theta = 1.2°$. (a) Single-particle band structure at $\Delta V = 20$ meV in valley K ($\tau = +$). The two central bands are separated by a direct gap, making the Chern number well defined for each band, but they have a negative indirect gap. (b) Valley polarization (VP), shown as color, and intervalley coherence (IVC) in the valley-filtered basis, shown with arrows, of the $\nu = +2$ CTI_1 state at $\Delta V = 20$ meV and $\epsilon_r = 16$ from 24×24 HF. Cyan (magenta) square denotes the Γ_M point of valley K (K') in (b)–(d). (c) The momentum-resolved overlap in valley K of the valley-filtered basis in (b) and the single-particle conduction basis. We observe that in some regions, the overlap vanishes because of mixing with the single-particle valence band, allowing the Chern number of the valley-filtered bands to differ from the single-particle conduction bands. (d) The direct band gap between the HF valence and conduction bands in valley K for a symmetry-preserving 16×16 HF calculation at $\nu = +2$. Comparing with (c), we observe that band hybridization occurs where the energy difference is small. For (b)–(d), we only show the quantities in one spin sector.

ies in the form of HF phase diagrams for each of the materials summarized in Table I in Sec. III, and close with a final discussion in Sec. IV.

TABLE I. Chern-textured exciton insulators (CTIs) in moiré materials studied in this work. The IVC order parameter winding is $4\pi n$ in the CTI_n phase. For $n = 0$, the state is considered a "trivial IVC" phase. [$t\mathrm{MoTe}_2$, twisted bilayer MoTe_2; TDBG, twisted double-bilayer graphene; TMBG, twisted mono-bilayer graphene; HTG, helical trilayer graphene; TBTG, twisted double-trilayer graphene (with AB-ABA stacking order); TSTG, twisted symmetric trilayer graphene; TBG, twisted bilayer graphene.]

System	$\hat{\mathcal{C}}_{2z}$-breaking	CTI_n index	Phase diag.
TDBG (ABAB)	explicit	2	Fig. 2
TDBG (ABBA)	explicit	0, 1, −1	Figs. 4 and 5
TMBG	explicit	0, 2	Fig. 7
TBTG	explicit	2	Fig. 8(b)
HTG	explicit	0, 1	Fig. 9
$t\mathrm{MoTe}_2$	explicit	0	Fig. 10(b)
TSTG	spontaneous	0	Fig. 11(b)

II. BACKGROUND, MODELS, AND METHODS

A. Chern texture insulators

The simplest setting in which a CTI can arise consists of a pair of Chern bands with Chern number $C_\tau = \tau n$, distinguished by a time-reversal-odd "valley" index $\tau = \pm 1$. The interacting Hamiltonian has time-reversal symmetry (TRS) $\hat{\mathcal{T}}$, which relates the two valleys, and $U_V(1)$ symmetry, i.e., the independent conservation of charge in each valley. In all the cases we study, the spin structure is such that we can choose the implementation of time reversal to satisfy $\hat{\mathcal{T}}^2 = +1$. The absence of a valley-exchanging $\hat{\mathcal{C}}_{2z}$ symmetry, whether because of explicit single-particle symmetry-breaking effects or interaction driven spontaneous symmetry breaking, is therefore crucial for allowing a nonzero valley Chern number [33]. In the limit where interactions dominate the kinetic energy, the ground state of the system at half-filling is expected to be a valley-polarized Chern insulator that breaks TRS [22,34,35].

In the intermediate-coupling regime where the kinetic energy is of similar magnitude as the interaction scale, we argued in Ref. [21] that a time-reversal-symmetric intervalley coherent insulator, which spontaneously breaks the $U_V(1)$ symmetry, is a generically competitive ground state. Spontaneous breaking of the $U_V(1)$ symmetry is characterized by the intervalley coherence (IVC) order parameter, defined as $\langle c^\dagger_{\boldsymbol{k},+} c_{\boldsymbol{k}',-}\rangle$, between the Bloch state with momentum $\boldsymbol{k}$ in valley $+$ and the Bloch state with momentum $\boldsymbol{k}'$ in valley $-$. If the ground state satisfies translation symmetry, the IVC order parameter is diagonal in momentum space, such that it may be written as $\Delta(\boldsymbol{k}) \equiv \langle c^\dagger_{\boldsymbol{k},+} c_{\boldsymbol{k},-}\rangle$. Because of the different Chern numbers $C_\pm = \pm n$ in the two valleys, the IVC order parameter $\Delta(\boldsymbol{k})$ acquires a $4\pi n$ winding as $\boldsymbol{k}$ winds around the Brillouin zone (BZ), when $c^\dagger_{\boldsymbol{k},\tau}$ is defined using a smooth gauge. This means, given a physically reasonable insulating state where $\Delta(\boldsymbol{k})$ is continuous within the BZ, $\Delta(\boldsymbol{k})$ must vanish at some points, called vortices, within the Brillouin zone. This leads to a nontrivial momentum-space "texture" in the IVC order parameter $\Delta(\boldsymbol{k})$. Furthermore, the valley polarization as a function of momenta $\boldsymbol{k}$ must also exhibit nontrivial behavior. To understand this, we consider the one-body density matrix $\rho_{\tau\tau'}(\boldsymbol{k}) \equiv \langle c^\dagger_{\boldsymbol{k},\tau} c_{\boldsymbol{k},\tau'}\rangle$. At half-filling for an insulating mean-field state, we can use Bloch sphere notation to write $\rho(\boldsymbol{k}) = \frac{1}{2}(I + \boldsymbol{n}\cdot\boldsymbol{\tau})$, where $\boldsymbol{\tau} = (\tau_x, \tau_y, \tau_z)$ denote Pauli matrices in valley space, and $\boldsymbol{n}$ is a valley pseudospin vector that satisfies $|\boldsymbol{n}| = 1$. At the vortices where IVC vanishes, $n_x = n_y = 0$ and we must have $n_z = \pm 1$. This means that the ground state fully valley polarizes at the cores of the IVC vortices. The resulting state is a Chern texture insulator denoted CTI_n, where the additional index n indicates the Chern number of the underlying valley-diagonal bands $C = \pm n$ (and hence fixes the enforced winding of the IVC order in the BZ to be $4\pi n$). In Ref. [21], we demonstrated that the CTI exhibits a form of delicate topology in an obstruction to an atomically localized limit. One further complication is that, in general, it is possible for IVC to develop between Bloch states with momentum $\boldsymbol{k}$ in valley $\tau = +$ and momentum $\boldsymbol{k} + \boldsymbol{q}$ in valley $\tau = -$, with $\boldsymbol{q}$ the wavevector of the resulting intervalley spiral order. The value of $\boldsymbol{q}$ realized in the ground state depends on the kinetic energy landscape of the system. Readers may find it helpful to

refer to Figs. 1(d) and 3(b) for visualizations of the IVC order parameter and the valley polarization of CTI states.

We note that there exists a $\mathcal{T}$-breaking cousin of the CTI that also exhibits a winding IVC across the BZ, but where the IVC vortex cores have the *same sense* of VP. This "tilted valley polarized" (TVP) phase has nonzero Chern number, yet is distinct on grounds of both symmetry and topology from the fully VP state, and is often found proximate to the CTI in the phase diagram of the toy models we have explored. Readers interested in details of the CTI and TVP and their topological properties beyond this brief account are directed to the companion paper, Ref. [21].

B. Continuum models

We perform self-consistent HF calculations on several moiré materials. To do so, we adopt the approach of first modeling the noninteracting moiré band structure within the "continuum model" approximation [36] and then incorporating Coulomb interactions projected to the resulting low-energy Hilbert space of the single-particle problem. In this subsection we describe the single-particle models for each of the different materials summarized in Table I, before turning to technical details of our HF computations in the next subsection.

1. Twisted double-bilayer graphene (ABAB)

Twisted double-bilayer graphene (TDBG) [30,31,37–46] is a heterostructure consisting of two Bernal (i.e., crystallographic AB or BA stacked) graphene bilayers placed on top of each other with a twist angle θ. Owing to the presence of Bernal bilayer stacks, the system does not possess $\hat{\mathcal{C}}_{2z}$ symmetry. The ABAB and ABBA stacking configurations are inequivalent; we first consider the former stacking order. In this case, the single-particle Hamiltonian for valley K is given by $H_K = H_{K,0} + H_V$, where the Hamiltonian in the absence of external displacement fields is [47–51]

$$H_{K,0} = \begin{pmatrix} H_0^A(\boldsymbol{k}_1) & g(\boldsymbol{k}_1) & & \\ g^\dagger(\boldsymbol{k}_1) & H_0^B(\boldsymbol{k}_1) & U & \\ & U^\dagger & H_0^A(\boldsymbol{k}_2) & g(\boldsymbol{k}_2) \\ & & g^\dagger(\boldsymbol{k}_2) & H_0^B(\boldsymbol{k}_2) \end{pmatrix}, \tag{1}$$

and we approximate the effect of an external displacement field with a linear interlayer potential [52]

$$H_V = \mathrm{diag}\big(-\tfrac{1}{2}I_2, -\tfrac{1}{6}I_2, \tfrac{1}{6}I_2, \tfrac{1}{2}I_2\big)\Delta V, \tag{2}$$

where I_2 is the 2×2 identity matrix in sublattice space. In Eq. (1), $\boldsymbol{k}_l = \boldsymbol{k} - \boldsymbol{K}_l$ is the momentum measured from the (rotated) Dirac point of layer $l = 1, 2$. With $k_\theta = \frac{8\pi}{3\sqrt{3}a_{\mathrm{CC}}}\sin(\theta/2)$ where $a_{\mathrm{CC}} = 1.42\times 10^{-10}$ m is the length of C-C bond, we define the primitive vectors of the moiré reciprocal lattice as $\boldsymbol{G}_1 = k_\theta(\sqrt{3}, 0)$ and $\boldsymbol{G}_2 = k_\theta(-\frac{\sqrt{3}}{2}, \frac{3}{2})$. The Dirac points of the two layers are related by $\boldsymbol{K}_1 - \boldsymbol{K}_2 = \frac{1}{3}\boldsymbol{G}_1 + \frac{2}{3}\boldsymbol{G}_2$. In Eq. (1), we also define

$$H_0 = v\boldsymbol{k}\cdot\boldsymbol{\sigma}, \tag{3}$$

$$H_0^A(\boldsymbol{k}) = H_0(\boldsymbol{k}) + \tfrac{1}{2}(I_2 - \sigma^z)\Delta', \tag{4}$$

$$H_0^B(\boldsymbol{k}) = H_0(\boldsymbol{k}) + \tfrac{1}{2}(I_2 + \sigma^z)\Delta', \tag{5}$$

$$g(\boldsymbol{k}) = \begin{pmatrix} -\hbar v_4 k_- & -\hbar v_3 k_+ \\ \gamma_1 & -\hbar v_4 k_- \end{pmatrix}, \tag{6}$$

where $\boldsymbol{\sigma} = (\sigma^x, \sigma^y)$ are the Pauli matrices in sublattice space, v is the graphene Fermi velocity, and $k_\pm = k_x \pm ik_y$. H_0^A and H_0^B capture the physics within each layer of graphene, and g represents hopping between the two layers within each Bernal bilayer stack. The parameters are given by $\gamma_0 = 2.610$ eV, $\gamma_1 = 0.361$ eV, $\gamma_3 = 0.283$ eV, $\gamma_4 = 0.138$ eV, and $\Delta' = 0.015$ eV [53]. The v_i's are related to the γ_i's by $v_i = \frac{3a}{2\hbar}\gamma_i$ and $v \equiv v_0$. The interlayer moiré coupling is

$$U = T_1 + T_2 e^{i(\boldsymbol{G}_1+\boldsymbol{G}_2)\cdot\boldsymbol{r}} + T_3 e^{i\boldsymbol{G}_2\cdot\boldsymbol{r}}, \tag{7}$$

where

$$T_{n+1} = w_{\mathrm{AA}} + w_{\mathrm{AB}}(\sigma^x\cos(n\phi) + \sigma^y\sin(n\phi)), \tag{8}$$

with $\phi = 2\pi/3$. We take $w_{AB} = 0.11$ eV, $w_{AA} = 0.08$ eV [36,54,55], and consider a twist angle $\theta = 1.2^\circ$ unless otherwise specified.

The continuum Hamiltonian in valley K' is determined by $H_{K'}(\boldsymbol{k}) = H_K^*(-\boldsymbol{k})$ because of TRS. Unless otherwise stated, we assume $SU(2)_{\mathrm{s}}$ spin-rotation symmetry for graphene-based materials because of the negligible spin-orbit coupling. An important exception is twisted homobilayer $MoTe_2$ in Sec. II B 6.

2. Twisted double-bilayer graphene (ABBA)

TDBG can also be fabricated in an alternative ABBA stacking arrangement [39,41,46]. Using the conventions established in the preceding subsection, the single-particle Hamiltonian in valley K is $H_K = H_{K,0} + H_V$, where $H_{K,0}$ is given by [47,48]

$$H_{K,0} = \begin{pmatrix} H_0^A(\boldsymbol{k}_1) & g(\boldsymbol{k}_1) & & \\ g^\dagger(\boldsymbol{k}_1) & H_0^B(\boldsymbol{k}_1) & U & \\ & U^\dagger & H_0^B(\boldsymbol{k}_2) & g^\dagger(\boldsymbol{k}_2) \\ & & g(\boldsymbol{k}_2) & H_0^A(\boldsymbol{k}_2) \end{pmatrix}, \tag{9}$$

and H_V is defined in Eq. (2). All single-particle parameters are identical to those used in the previous subsection.

3. Twisted monolayer-bilayer graphene

Twisted monolayer-bilayer graphene (TMBG) [32,56–61] is $\hat{\mathcal{C}}_{2z}$-breaking heterostructure that consists of one graphene monolayer and one Bernal graphene bilayer stacked together with a twist. Using the conventions established in Sec. II B 1, the single-particle Hamiltonian for TMBG in valley K is given by [48,62]

$$H_K = \begin{pmatrix} H_0(\boldsymbol{k}_1) - \frac{1}{2}\Delta V & U & \\ U^\dagger & H_0^A(\boldsymbol{k}_2) & g(\boldsymbol{k}_2) \\ & g^\dagger(\boldsymbol{k}_2) & H_0^B(\boldsymbol{k}_2) + \frac{1}{2}\Delta V \end{pmatrix}. \tag{10}$$

All single-particle parameters are identical to those in Sec. II B 1.

4. Twisted bilayer-trilayer graphene

Twisted bilayer-trilayer graphene (TBTG) [63] is a $\hat{\mathcal{C}}_{2z}$-breaking heterostructure consisting of a Bernal-stacked graphene bilayer placed on top of a Bernal-stacked graphene trilayer with a twist angle θ. In this work, we only consider the AB-ABA stacking configuration. The single-particle Hamiltonian for valley K is given by $H_K = H_{K,0} + H_V$, where the Hamiltonian in the absence of external displacement fields is [48,62]

$$H_{K,0} = \begin{pmatrix} H_0^A(\boldsymbol{k}_1) & g(\boldsymbol{k}_1) & & & \\ g^\dagger(\boldsymbol{k}_1) & H_0^B(\boldsymbol{k}_1) & U & & \\ & U^\dagger & H_0^A(\boldsymbol{k}_2) & g(\boldsymbol{k}_2) & \\ & & g^\dagger(\boldsymbol{k}_2) & H_0^B(\boldsymbol{k}_2) & g^\dagger(\boldsymbol{k}_2) \\ & & & g(\boldsymbol{k}_2) & H_0^A(\boldsymbol{k}_2) \end{pmatrix}, \tag{11}$$

and the interlayer potential is given by

$$H_V = \mathrm{diag}\left(-\tfrac{1}{2}I_2, -\tfrac{1}{4}I_2, 0, \tfrac{1}{4}I_2, \tfrac{1}{2}I_2\right)\Delta V. \tag{12}$$

All single-particle parameters are identical to those in Sec. II B 1.

5. Helical trilayer graphene

Helical trilayer graphene (HTG) is a supermoiré material that consists of three layers of graphene that are rotated consecutively with identical twist angles θ. While HTG preserves $\hat{\mathcal{C}}_{2z}$ on the global scale, relaxation calculations show that it relaxes into large moiré-periodic domains (referred to as h-HTG and $\bar{\text{h}}$-HTG) of linear dimension $\sim$100 nm (near the magic angle $\theta \sim 1.8^\circ$), that individually break $\hat{\mathcal{C}}_{2z}$ and are mapped into each other under $\hat{\mathcal{C}}_{2z}$ [64–66]. The interacting physics of HTG can then be understood by focusing on the properties of the individual domains.

We closely follow the conventions of Ref. [67]. Considering valley K and h-HTG without loss of generality, the continuum Hamiltonian is $H_K = H_{K,0} + H_V$, where

$$H_{K,0} = \begin{pmatrix} -iv_F\boldsymbol{\sigma}\cdot\boldsymbol{\nabla} & T(\boldsymbol{r}-\boldsymbol{d}_t) & 0 \\ T^\dagger(\boldsymbol{r}-\boldsymbol{d}_t) & -iv_F\boldsymbol{\sigma}\cdot\boldsymbol{\nabla} & T(\boldsymbol{r}-\boldsymbol{d}_b) \\ 0 & T^\dagger(\boldsymbol{r}-\boldsymbol{d}_b) & -iv_F\boldsymbol{\sigma}\cdot\boldsymbol{\nabla} \end{pmatrix} \tag{13}$$

with $v_F = 8.8\times10^5\,\mathrm{ms}^{-1}$, and $H_V = \mathrm{diag}(-1/2, 0, 1/2)\,\Delta V$. Note that the wavefunction in each layer is written relative to its Dirac point (this is very slightly strained to accommodate a moiré periodicity), and as a consequence the relevant interlayer tunneling are shifted by $\boldsymbol{d}_{t,b}$ in the top and bottom layer. The unshifted tunneling matrix is given by [68]

$$T(\boldsymbol{r}) = \begin{pmatrix} w_{AA}t_0(\boldsymbol{r}) & w_{AB}t_{-1}(\boldsymbol{r}) \\ w_{AB}t_1(\boldsymbol{r}) & w_{AA}t_0(\boldsymbol{r}) \end{pmatrix},$$

$$t_\alpha(\boldsymbol{r}) = \sum_{n=0}^{2} e^{\frac{2\pi i}{3}n\alpha} e^{-i\boldsymbol{q}_n\cdot\boldsymbol{r}},$$

$$q_{n,x} + iq_{n,y} = -ik_\theta e^{\frac{2\pi i}{3}n}, \tag{14}$$

where $\boldsymbol{K}_{1,3} = \mp\boldsymbol{q}_0 + \boldsymbol{K}_2$. We use $w_{AA} = 75$ meV and $w_{AB} = 110$ meV. The relative shifts of the layers in h-HTG are parameterized by $\boldsymbol{d}_t - \boldsymbol{d}_b = \boldsymbol{\delta} = \frac{1}{3}(\boldsymbol{a}_2 - \boldsymbol{a}_1)$, where $\boldsymbol{a}_{1,2} = \frac{4\pi}{3k_\theta}(\pm\frac{\sqrt{3}}{2}, \frac{1}{2})$.

6. Twisted homobilayer $MoTe_2$

We closely follow the conventions of Refs. [70,71] in our description of the continuum model [72] for the valence bands of AA-stacked homobilayer $MoTe_2$ with small twist angle ($t\mathrm{MoTe}_2$). This system also lacks $\hat{\mathcal{C}}_{2z}$, and owing to strong spin-orbit coupling, the valence bands are spin-valley locked such that $\tau = +$ ($\tau = -$) is tied to spin-$\uparrow$ (spin-$\downarrow$). In valley K, the rotated K point of the top layer is at $\boldsymbol{K}_t = \frac{4\pi}{3a_0}(\cos\theta/2, -\sin\theta/2)$, while that of the bottom layer is at $\boldsymbol{K}_t = \frac{4\pi}{3a_0}(\cos\theta/2, \sin\theta/2)$, where $a_0 = 0.352$ nm is the lattice constant. In terms of $\boldsymbol{q}_1 = \boldsymbol{K}_b - \boldsymbol{K}_t$, we have the basis moiré RLVs $\boldsymbol{b}_1 = (\hat{\mathcal{C}}_3^2 - \hat{\mathcal{C}}_3)\boldsymbol{q}_1$ and $\boldsymbol{b}_2 = -\hat{\mathcal{C}}_3^2\boldsymbol{b}_1$, where $\hat{\mathcal{C}}_3$ is a counterclockwise rotation by $2\pi/3$.

In layer space, the real-space continuum Hamiltonian takes the form

$$H_K = \begin{pmatrix} h_{\tau,b}(\boldsymbol{r}) & t_\tau(\boldsymbol{r}) \\ t_\tau^*(\boldsymbol{r}) & h_{\tau,t}(\boldsymbol{r}) \end{pmatrix}. \tag{15}$$

The intralayer term (in a layer-dependent frame centered at the corresponding Dirac momentum) is

$$h_{\tau,l}(\boldsymbol{r}) = \frac{\hbar^2\nabla^2}{2m^*} + V_{\tau,l}(\boldsymbol{r}) + (-1)^l\frac{\Delta V}{2}, \tag{16}$$

where m^* is the effective mass. The intralayer moiré potential $V_{\tau,l}(\boldsymbol{r})$ and interlayer hopping $t_\tau(\boldsymbol{r})$ are, at the first harmonic level, given by

$$V_{\tau,l}(\boldsymbol{r}) = Ve^{-(-1)^l i\psi}\sum_{i=1,2,3} e^{i\boldsymbol{g}_i\cdot\boldsymbol{r}} + \text{c.c.} \tag{17}$$

$$t_\tau(\boldsymbol{r}) = w\sum_{i=1,2,3} e^{-i\tau\boldsymbol{q}_i\cdot\boldsymbol{r}}, \tag{18}$$

where $(-1)^t = 1$ and $(-1)^b = -1$, and $\boldsymbol{g}_i = \hat{\mathcal{C}}_3^{i-1}\boldsymbol{b}_1$.

In the main text, we focus on twist angles $\theta = 3.4^\circ - 4.0^\circ$, and use the parameters of Ref. [73], i.e., $m^* = 0.6m_e$, $w = -23.8$ meV, $V = 20.8$ meV, $\psi = -107.7^\circ$. We have also checked that our conclusions on the nature of the IVC state remain unchanged using the parameters of Ref. [74], i.e., $m^* = 0.62m_e$, $w = -13.3$ meV, $V = 11.2$ meV, $\psi = -91^\circ$. However, we have not exhaustively explored the extended parameter space of the relevant models in full, leaving this as a subject for future work.

7. Twisted symmetric trilayer graphene

Twisted symmetric trilayer graphene (TSTG) [4,18,28,75–84] is a $\hat{\mathcal{C}}_{2z}$-symmetric heterostructure that consists of three

sheets of monolayer graphene stacked together, with the middle layer twisted by θ relative to the top and bottom layers. Using the conventions established in Sec. II B 1, the single-particle Hamiltonian for TSTG in valley K is given by [85–87]

$$H_K = \begin{pmatrix} H_0(\boldsymbol{k}_1) - \frac{1}{2}\Delta V & U & \\ U^\dagger & H_0(\boldsymbol{k}_2) & U^\dagger \\ & U & H_0(\boldsymbol{k}_1) + \frac{1}{2}\Delta V \end{pmatrix}. \quad (19)$$

We use $w_{AB} = 0.11$ eV, $w_{AA} = 0.075$ eV, $\gamma_0 = 2.73$ eV (which defines the graphene Fermi velocity as $v = \frac{3a}{2\hbar}\gamma_0$) and twist angle $\theta = 1.56^\circ$.

C. Details of Hartree-Fock calculations

We will be interested in electronic filling factors ν near charge neutrality, which corresponds to $\nu = 0$. Since interaction-induced phenomena primarily involve just a few low-energy moiré bands, which are often energetically separated from higher "remote" bands, we project our calculations into a subset of "active" bands. These are associated with band creation operators $c^\dagger_{\boldsymbol{k},f,a}$, where $\boldsymbol{k}$ is a momentum in the moiré BZ (mBZ), f is a spin-valley flavor index, and a is a band index. For both variants of TDBG, TMBG, TBTG, and h-HTG, we take the active bands to be the central two moiré bands per spin and valley. For $t\mathrm{MoTe}_2$, we project onto the highest three valence bands per valley. For TSTG, we project onto the central four bands per spin and valley.

For the interaction part of the Hamiltonian, we include density-density interactions with gate-screened Coulomb potential $V(q) = (e^2/2\epsilon_0\epsilon_r q)\tanh qd_{\mathrm{sc}}$, where d_{sc} is the screening length. For both variants of TDBG, TMBG, TBTG, h-HTG, and TSTG, we use $d_{\mathrm{sc}} = 25$ nm. For $t\mathrm{MoTe}_2$, we use $d_{\mathrm{sc}} = 10$ nm. To capture the uncertainty in the interaction strength, we take the relative permittivity ϵ_r to be a variable parameter.

The band-projected interacting Hamiltonian is given by

$$\mathcal{H} = \sum_{\boldsymbol{k}\in\mathrm{BZ},\alpha} \epsilon_{\boldsymbol{k},\alpha} c^\dagger_{\boldsymbol{k},\alpha} c_{\boldsymbol{k},\alpha} + \frac{1}{2A}\sum_{\boldsymbol{q}} V(\boldsymbol{q}) :\rho_{\boldsymbol{q}}\rho_{-\boldsymbol{q}}: \quad (20)$$

where α is a combined flavor and band index, $\epsilon_{\boldsymbol{k},\alpha}$ is the single-particle dispersion, and $\rho_{\boldsymbol{q}}$ is the projected density operator defined as

$$\rho_{\boldsymbol{q}} = \sum_{\boldsymbol{k}\in\mathrm{BZ}} \langle u_{\boldsymbol{k},\alpha}|u_{\boldsymbol{k}+\boldsymbol{q},\beta}\rangle\, c^\dagger_{\boldsymbol{k},\alpha} c_{\boldsymbol{k}+\boldsymbol{q},\beta}, \quad (21)$$

with $|u_{\boldsymbol{k},\beta}\rangle$ denoting the mBZ-periodic part of the single-particle wavefunctions. The double colons :: denote normal-ordering with a special procedure to avoid double-counting, as discussed below.

To avoid double-counting interactions, when writing down the quartic Coulomb coupling we normal order with respect to a background or reference density matrix P^{ref}, that describes the "vacuum" state around which we measure charge fluctuations. For both variants of TDBG, TMBG, TBTG, and h-HTG, P^{ref} consists of occupied remote valence bands, and occupation of $1/2$ within the active central bands (this is an example of the so-called "average" scheme). For $t\mathrm{MoTe}_2$, the reference density matrix corresponds to filling the valence bands to charge neutrality. For TSTG, the two central bands have occupation $1/2$ and the remote valence bands are occupied in P^{ref}. We have also studied some materials using an alternative subtraction scheme, termed the "graphene" scheme, and the results are presented in the Supplemental Material [69] (see also Ref. [88] therein). While the overall conclusions are not affected by the choice of subtraction scheme, we note that the precise parameters for which various phases are stabilized show some dependence on the choice of subtraction scheme.

We address the resulting interacting problem using self-consistent Hartree-Fock (HF) mean field simulations. Self-consistent HF involves finding the lowest-energy state within the manifold of Slater determinants. For simplicity, we use $i, j, \ldots$ as combined indices for momentum, flavor, and single-particle band, and write the two-body interaction as $V_{ijkl} = \langle ij|\hat{V}|kl\rangle$. The HF Hamiltonian can be written as

$$H^{\mathrm{HF}}[P] = \sum_i \epsilon_i c^\dagger_i c_i + \sum_{ijkl}(P_{kl} - P^{\mathrm{ref}}_{kl})(V_{ikjl} - V_{ikl\,j})c^\dagger_i c_j \quad (22)$$

where $P_{ij} = \langle c^\dagger_i c_j\rangle$ is the single-particle density matrix and P^{ref} is the reference density matrix as discussed above. Starting from an initial seed density matrix, this Hamiltonian is solved iteratively until convergence. We minimize over multiple initial seeds to find the HF ground state.

HF has been shown to be a versatile and reliable tool for addressing the physics of moiré materials at or near integer fillings. The effectiveness of HF can be motivated in part from strong coupling [89–91], where, for example, in the case of TBG it is possible to show that it is exact in certain specialized limits in which the ground states are exact Slater determinants. Indeed, in cases where it has been possible to compare against alternative beyond-mean field approaches such as exact diagonalization or density-matrix renormalization group (DMRG), these have often shown good agreement with the HF, which is numerically far less costly for a given system size. For example, DMRG studies of strained TBG at integer filling $\nu = -3$ [92] find IKS order whose properties are consistent with those of the mean-field state originally identified using HF in Ref. [26].

For the graphene-based moiré materials, we restrict to spin-collinear calculations, i.e., we constrain the density matrix $P_{f,a;f',b}(\boldsymbol{k},\boldsymbol{k}') = \langle c^\dagger_{\boldsymbol{k},f,a} c_{\boldsymbol{k}',f',b}\rangle$ to be diagonal in spin. Since we are interested in valley spirals, we enforce a generalized translation invariance parameterized by a boost wavevector $\boldsymbol{q}$. This means that IVC is only permitted at wavevector $\boldsymbol{q}$, such that $\boldsymbol{k}$ in valley $\tau = +$ hybridizes with $\boldsymbol{k}+\boldsymbol{q}$ in valley $\tau = -$, leading to an intervalley spiral. On the other hand, valley-diagonal observables yield moiré translation-invariant expectation values. We perform calculations over a range of $\boldsymbol{q}$, and select the HF solution with the lowest energy. For both variants of TDBG, TBTG, and TMBG, we sweep over all values of $\boldsymbol{q}$ on the momentum grid. For all other materials, we restrict to $\hat{\mathcal{C}}_{3z}$-symmetric boosts $\boldsymbol{q} = \Gamma_M, K_M, K'_M$ for simplicity.

III. RESULTS

A. Twisted double-bilayer graphene (ABAB)

As shown in Fig. 1(a), the single-particle band structure of TDBG with ABAB stacking order at $\theta = 1.2^\circ$ has

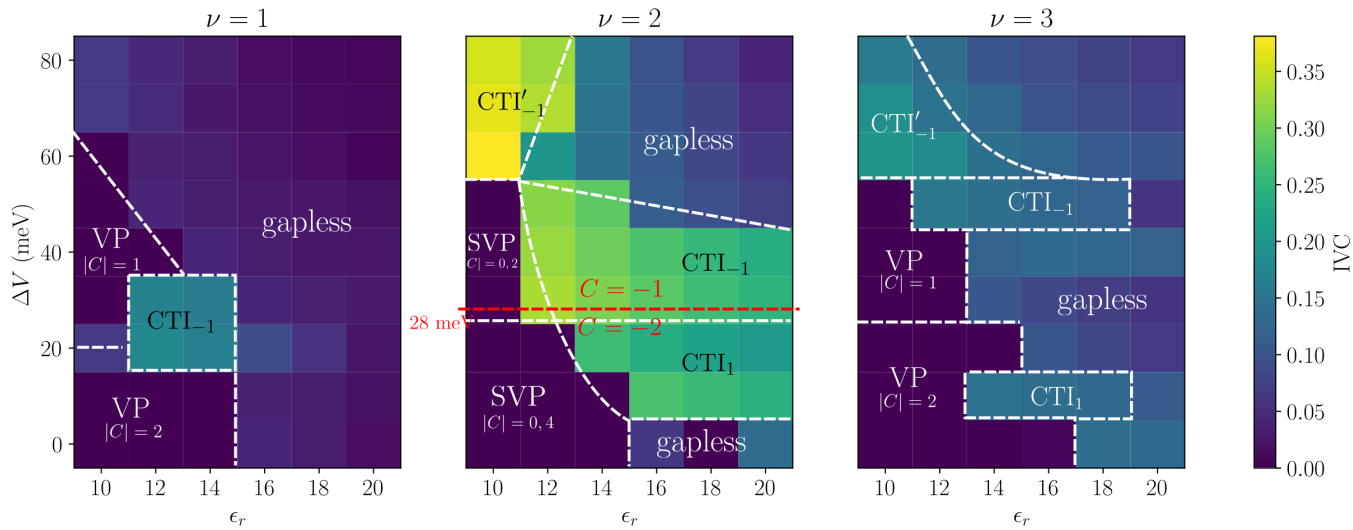


FIG. 4. Phase diagram of ABBA-stacked twisted double-bilayer graphene (TDBG) at $\theta = 1.2°$. The results are obtained using 12×12 HF at $\nu = 1, 2, 3$. VP denotes valley-polarized states, which also carry a nonzero spin polarization. SVP denotes spin- or valley-polarized states, which are degenerate in HF. TVP denotes tilted-valley-polarized states. Topological transitions in the noninteracting band structure are marked in red, with the Chern number refers to that of the central conduction band. CTI′ has a different intervalley spiral wavevector $\boldsymbol{q}$ from the unprimed CTI states.

well-isolated Chern bands with $|C| = 2$ under moderate interlayer potential ΔV [35,47,48]. Within this window of ΔV, self-consistent HF calculations at $\nu = 1, 2, 3$ find flavor-polarized strong-coupling insulators at strong interaction strengths (i.e., small relative permittivity ϵ_r), as shown in Fig. 2. For weaker interactions, we find a greater tendency towards gapless metallic phases. However, for all the fillings investigated here, we obtain insulating CTIs for a window of finite interlayer potentials.

We now focus on $\nu = 2$, where the CTI is observed over a large region of parameter space. The behavior of the CTI at $\nu = 2$ is identical in both spin sectors, so we only show results for one spin sector. With electron doping and well-separated conduction and valence bands, we expect the nontrivial physics to occur within the noninteracting conduction bands. As such, we define the IVC order parameter $\Delta_{\boldsymbol{q}}(\boldsymbol{k})$ as

$$\Delta_{\boldsymbol{q}}(\boldsymbol{k}) \equiv \langle c^{\dagger}_{\boldsymbol{k},+} c_{\boldsymbol{k}+\boldsymbol{q},-} \rangle \tag{23}$$

where $c^{\dagger}_{\boldsymbol{k}\tau}$ is the spin-up electron creation operator in the conduction band of valley τ. The order parameter, shown in Fig. 1(d), shows vortices with 8π-winding around the moiré Brillouin zone (mBZ), which is topologically required because of the Chern numbers $C = \pm 2$ of the constituent conduction bands. This leads us to identify the phase as a CTI_2. We note that the vorticity is carried by two vortices with winding number 2. While the order parameter is dependent on the gauge choice [93], we also define the gauge-independent velocity as

$$\boldsymbol{j}_{\boldsymbol{k}} = \nabla\theta_{\boldsymbol{k}} + \boldsymbol{A}_{\boldsymbol{k},+} - \boldsymbol{A}_{\boldsymbol{k}+\boldsymbol{q},-} \tag{24}$$

where $\theta_{\boldsymbol{k}} = \arg(\Delta_{\boldsymbol{q}}(\boldsymbol{k}))$ is the angle of the IVC order parameter and $\boldsymbol{A}_{\boldsymbol{k}\tau} = i\langle u_{\boldsymbol{k}\tau} | \partial_{\boldsymbol{k}} u_{\boldsymbol{k}\tau} \rangle$ is the Berry-connection. As shown in Fig. 1(c), the velocity diverges near the vortices, which is compensated by the vanishing IVC order parameter. In addition to the CTI_2, we have also found a sliver of the tilted valley-polarized (TVP) phase [Fig. 1(b)], which was introduced in Ref. [21].

The physics of CTI in $\nu = 1, 3$ is essentially identical to that in $\nu = 2$, except that for these odd integer fillings, IVC is only present in one of the two spin sectors (namely, the spin sector with filling factor 1 relative to its charge neutrality). We note that the interaction-induced band normalization depends on the total filling, leading to the CTI being found at different regions of parameter space for different fillings. We further note that at $\nu = 1, 3$, we find the CTI to be the only energetically competitive candidate for a ground state with a zero Chern number at finite interlayer potential. Therefore, we believe that experimentally observed $C = 0$ correlated insulators at these fillings, such as in Ref. [40] at $\nu = 3$, have a natural explanation in terms of the CTI.

B. Twisted double-bilayer graphene (ABBA)

Similar to ABAB-stacked TDBG, we observe the presence of CTIs at all of $\nu = 1, 2, 3$ for ABBA-stacked TDBG (Fig. 4). We again focus on $\nu = +2$, which contains the largest region of gapped IVC insulators. However, we observe some complications not present in the simplest setting with just one band per valley. As discussed in the previous subsection, in the regime where the CTI is observed in $\nu = +2$ ABAB-stacked TDBG, the conduction band is sufficiently separated from the valence band and other remote bands to prevent them from participating nontrivially in the IVC. In ABBA-stacked TDBG, at a small interlayer potential of $\Delta V = 20$ meV, the central conduction bands are also topological with $|C| = 2$ [47,48], but they can significantly mix with the central valence bands owing to the lack of clear energetic separation [Fig. 3(a)].

To understand the nature of intervalley coherent phases obtained in HF calculations in such cases, we consider the following valley-filtered basis. If the HF spectrum contains an isolated [94] IVC band above or below E_F (within a spin sec-

tor), we can unfold this HF band $|\mathrm{HF}, \boldsymbol{k}\rangle$ into two normalized valley-diagonal bands $|\mathrm{HF}_+, \boldsymbol{k}\rangle$ and $|\mathrm{HF}_-, \boldsymbol{k}\rangle$,

$$|\mathrm{HF}, \boldsymbol{k}\rangle = \alpha(\boldsymbol{k})\,|\mathrm{HF}_+, \boldsymbol{k}\rangle + \beta(\boldsymbol{k})\,|\mathrm{HF}_-, \boldsymbol{k}\rangle\,. \tag{25}$$

For the IVC states in ABBA-stacked TDBG at $\nu = 2$, we define the valley-filtered basis using the unfilled HF band immediately above E_F in each spin sector, since it is isolated from the filled bands and higher remote conduction bands by charge gaps (the latter do not mix with the central bands in any significant way). We note that the valley-filtered basis for a CTI defined using Eq. (25) is ambiguous at discrete points in each valley where $|\mathrm{HF}, \boldsymbol{k}\rangle$ is fully polarized into the other valley, but this can be resolved by assuming that the valley-filtered basis is continuous in $\boldsymbol{k}$ space. We also comment that even though we extract the valley-filtered basis from an unfilled HF band, we continue to define the order parameter as $\Delta_{\boldsymbol{q}}(\boldsymbol{k}) \equiv \langle c^\dagger_{\boldsymbol{k},+} c_{\boldsymbol{k}+\boldsymbol{q},-}\rangle$, where $c^\dagger_{\boldsymbol{k}\tau}$ are *electron* creation operators for the valley-filtered basis [95].

At $\Delta V = 20$ meV, the single-particle conduction band has Chern number $C = -2$ $(+2)$ in valley K (K'), while the valence bands are trivial. For strong interactions, HF calculations at $\nu = +2$ find flavor-polarized insulators (Fig. 4). For weaker interactions, we find a $\hat{\mathcal{T}}$ and $SU(2)_s$-symmetric IVC insulator [96]. However, the corresponding valley-filtered basis is found to have $C = +1$ (-1) in valley K (K'), which differs from that of the single-particle conduction bands; and the IVC order parameter winds by 4π instead of -8π around the mBZ [Fig. 3(b)]. This means that we obtain a CTI_1, instead of a CTI_{-2} that would be naïvely expected by considering the noninteracting band topology. In Fig. 3(c), we plot the overlap of the valley-filtered band with the single-particle conduction band, which vanishes at three $\hat{\mathcal{C}}_{3z}$-related points in the mBZ. This allows the valley Chern number of the valley-filtered basis to differ from that of the single-particle conduction basis.

We note that the absolute value of the valley-filtered basis Chern number is lowered from 2 to 1. This is consistent with the notion that there is a tendency to reduce the winding (i.e., "unfrustrate" the topological obstruction) of the order parameter, since this allows more favorable exchange energetics. The system achieves this by substantially hybridizing with the single-particle valence band. Because of the kinetic energy penalty, such hybridization preferentially occurs at regions with small direct gap. We can roughly estimate the hybridization positions by performing symmetry-preserving HF at this filling, which partially accounts for interaction-induced renormalization effects [Fig. 3(d)]. In this specific example, the hybridization occurs away from high-symmetry points. This restricts the valley-filtered basis Chern number to change by multiples of 3 [97], which does not permit a full lifting of the topological frustration. For larger ΔV, we observe additional CTI_n phases, including two CTI_{-1} regions with distinct $\boldsymbol{q}$, highlighting the complex interplay between the kinetic energy and interaction-induced effects.

We have also performed HF calculations at $\nu = 2$ for different twist angles θ to confirm that the CTI in ABBA-stacked TDBG is stable under a range of twist angles (Fig. 5).

C. Twisted monolayer-bilayer graphene

Twisted monolayer-bilayer graphene (TMBG) is similar to ABAB-stacked TDBG in that it realizes an isolated

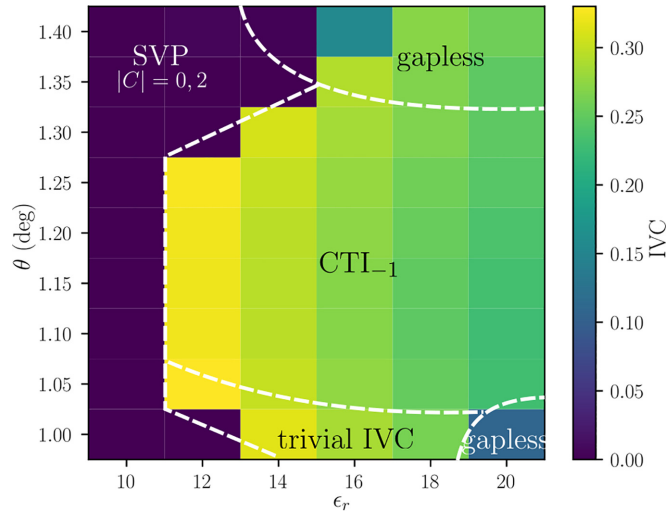


FIG. 5. Phase diagram of ABBA-stacked twisted double-bilayer graphene (TDBG) with variable twist angle. The results are obtained using 12×12 HF at $\nu = 2$ and $\Delta V = 40$ meV. SVP denotes spin- or valley-polarized states, which are degenerate in HF. We observe that the CTI is stable under a range of twist angles.

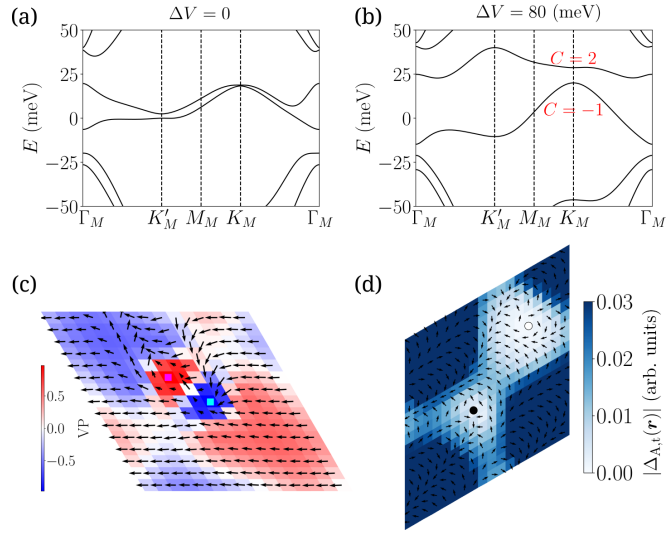


FIG. 6. Twisted monolayer-bilayer graphene (TMBG) at $\theta = 1.2°$. (a) Single-particle band structure at zero interlayer potential. The direct gap between the two central bands is nearly vanishing. (b) At finite interlayer potential of $\Delta V = 80$ (meV), the conduction and valence bands are well isolated with Chern numbers 2 and -1, respectively. (c) The *momentum-space* valley polarization (VP), shown as color, and intervalley coherence (IVC) in the valley-filtered basis, shown with arrows, of the $\nu = +2$ trivial IVC state at $\Delta V = 0$ and $\epsilon_r = 12$ in 15×15 HF. Cyan (magenta) square denotes the Γ_M point of valley K (K'). (d) The same state as in (c), but showing the *real-space* IVC order parameter *within* a moiré unit cell for sublattice A on the top layer. The color shows the IVC magnitude and the arrows show the IVC phase angle, where we have subtracted off the spiral modulation owing to finite $\boldsymbol{q}$. There is a vortex-antivortex pair, labeled with black and white circles. Note that the upper limit of the color scale has been clamped to show the regions near vortices more clearly.

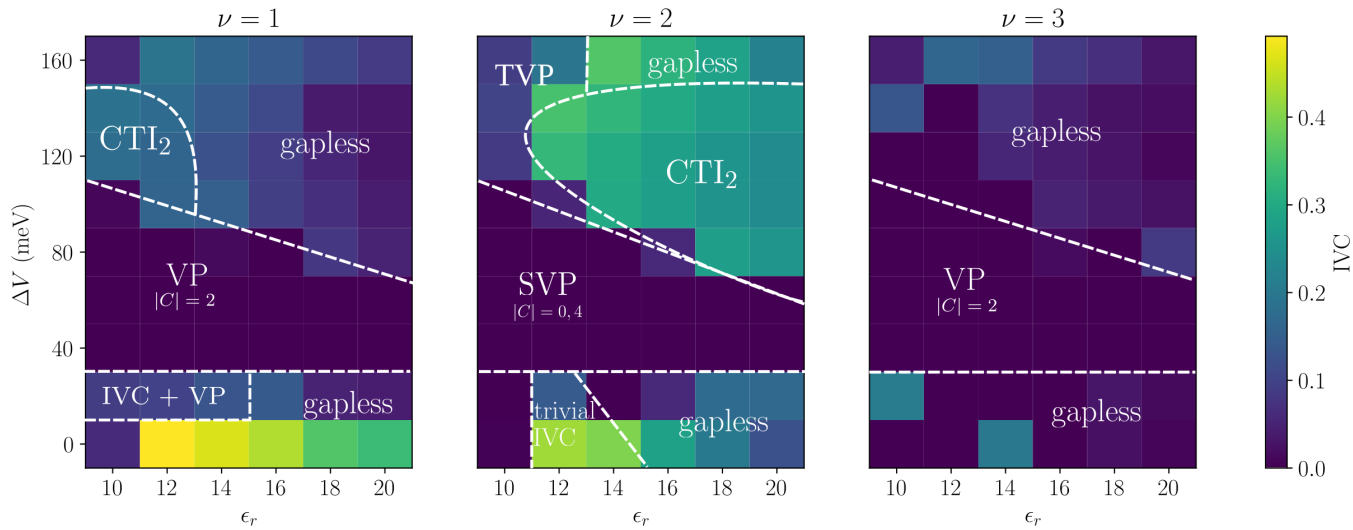


FIG. 7. Phase diagram of twisted monolayer-bilayer graphene (TMBG) at $\theta = 1.2°$. The results are obtained using 12×12 HF at $\nu = 1, 2, 3$. VP denotes valley-polarized states, which also carry a non-zero spin polarization. SVP denotes spin- or valley-polarized states, which are degenerate in HF. TVP denotes tilted-valley-polarized states. IVC + VP denotes a state that is IVC in one spin sector and VP in the other spin sector.

conduction band with valley Chern number 2 at finite interlayer potential [48,62] (Fig. 6). Its phase diagram is shown in Fig. 7. We find regions of CTI_2 at moderately high interlayer potential ΔV for $\nu = 1, 2$. At lower interlayer potentials, we also find a trivial IVC insulator with TRS at $\nu = 2$, where "trivial" means that the valley-filtered bands have vanishing Chern number [Fig. 6(c)]. This allows the IVC to be nonvanishing across the mBZ. For such small ΔV, the noninteracting conduction and valence bands are not isolated [Fig. 6(a)], leading to strong inter-band hybridization, which alleviates the IVC-related obstructions.

We stress that the IVC vortices discussed so far are momentum-space vortices, which are distinct from possible vortices in the real-space IVC order parameter. We define the latter as $\Delta_f(\boldsymbol{r}) = \langle \psi^\dagger_{+,f}(\boldsymbol{r})\psi_{-,f}(\boldsymbol{r})\rangle$, where $+, -$ are valley labels and f indexes other degrees of freedom such as sublattice or layer. For the trivial IVC state in TMBG, we consider the real-space order parameter on sublattice A of the top layer, and observe a vortex and antivortex within the moiré unit cell [Fig. 6(d)]. Hence, we conclude that the presence or absence of real-space IVC vortices cannot be directly used to discriminate between a CTI and a trivial-IVC state. However, detailed scanning of the intra-moiré cell IVC pattern is still invaluable in providing evidence for the existence of specific IVC states, as was done for the IKS in TBG in Ref. [27]. In Ref. [57], insulating states with vanishing Chern number $C = 0$ were experimentally observed in TMBG at $\nu = 1$ with finite displacement field in multiple devices with twist angles $\theta \simeq 1.1° - 1.2°$. Since a fully flavor polarized state is expected to have a nonzero Chern number owing to the single-particle band structure, while the CTI states have zero Chern number, this indirectly supports a CTI state. The theoretically calculated valley magnon instability with finite momentum transfer in Ref. [57] is also consistent with the finite-$\boldsymbol{q}$ nature of our proposed CTI state. Further, the experimental signature of time-reversal symmetry-breaking upon hole doping away from $\nu = 1$ [57] is consistent with our Hartree-Fock analysis [98], and does not contradict the time-reversal-symmetric nature of the state at the integer filling.

D. Twisted bilayer-trilayer graphene

In Ref. [63], the authors experimentally found insulating states with Chern number 0 in twisted bilayer-trilayer graphene (TBTG) with stacking order AB-ABA at $\nu = 1$ in the presence of a displacement field and a small perpendicular magnetic field. As shown in Fig. 8(a), with applied interlayer potential, the conduction band in valley K has a Chern number of 2, suggesting that the observed Chern number 0 state cannot be a valley polarized state. On the other hand, the CTI, being time-reversal invariant, is consistent with the measurement. To investigate this, we performed HF calculations of TBTG at $\nu = 1$ without a magnetic field. We found a CTI phase with a high interlayer potential and relatively strong interaction, as shown in Fig. 8(b), while large regions of the phase diagram show gapless ground states (though we note that the CTI phase cannot be stabilized with the "graphene" subtraction

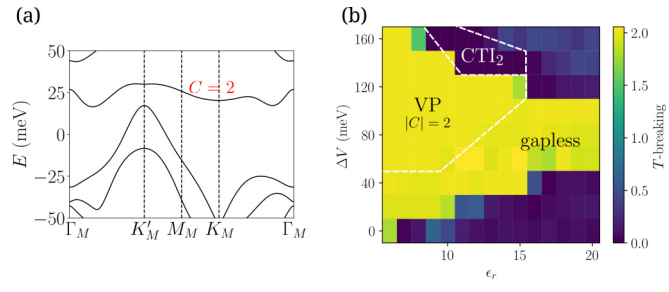


FIG. 8. Twisted bilayer-trilayer graphene (TBTG) at $\theta = 1.5°$. (a) Single-particle band structure at $\Delta V = 120$ meV in valley K. The valence band highly dispersive while the conduction band is moderately flat with a Chern number 2. (b) Phase diagram from 12×12 HF at $\nu = 1$. VP denotes valley-polarized states, which also carry a nonzero spin polarization.

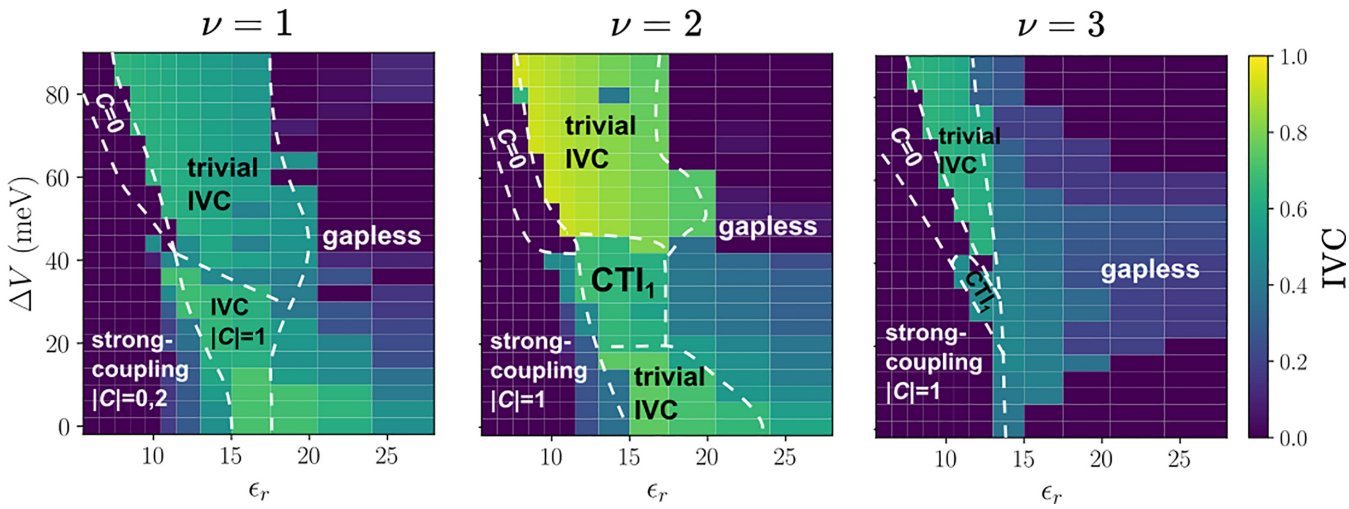


FIG. 9. Phase diagram of helical trilayer graphene (HTG) at $\theta = 1.85°$. We focus on one h-HTG domain. Phase diagram calculated using 12×12 HF at $\nu = 1, 2, 3$. Momentum-dependent tunneling terms are not included.

scheme in the same parameter region, as shown in Ref. [69]). We speculate that the application of a perpendicular magnetic field, through Zeeman splitting and orbital reconstruction, is responsible for further favoring gapped-CTI states over gapless states.

E. Helical trilayer graphene

Helical trilayer graphene (HTG) is a supermoiré platform that hosts large-scale moiré-periodic domains whose isolated central bands carry strong-coupling valley Chern numbers of up to 2 [64–66,99]. While HTG preserves $\hat{\mathcal{C}}_{2z}$ at the global scale, the domains (labelled h-HTG and $\bar{\text{h}}$-TTG) individually break $\hat{\mathcal{C}}_{2z}$. The presence of Kekulé spirals with a commensurate IVC wavevector $\boldsymbol{q}$ was previously reported in HF studies at finite ΔV [67].

In Fig. 9, we show the phase diagram in the h-HTG domain of helical trilayer graphene at $\theta = 1.85°$. For strong interactions (small ϵ_r), we have the "strong-coupling" phase, which can be understood by fully occupying certain spin- and valley-diagonal Chern bands [67]. Near the phase boundary to the intermediate-coupling phases, there can be small amounts of IVC arising from momentum-localized excitonic instabilities. For $\epsilon \sim 15$ and $\nu = +2$, we find three gapped IVC phases that preserve TRS. The two phases for small and large interlayer potential ΔV have trivial IVC, as diagnosed by the nonvanishing of IVC across the mBZ, and the fact that the valley-filtered basis has $C = 0$. For intermediate ΔV, we find a CTI_1 phase. For weaker interactions, HF yields gapless phases. We note that a CTI_2 can be obtained by applying an artificially large sublattice potential (projected to the central bands). This is because the Chern basis bands with predominant weight on sublattice B (A) have $|C| = 2$ ($|C| = 1$). Hence, by applying a large enough sublattice potential, the B bands can be sufficiently separated from the A bands so as to prevent interaction-induced mixing, and to allow a CTI_2 constructed from the B bands.

For $\nu = 3$, we find a much narrower CTI_1 region, while for $\nu = 1$, we do not find any CTIs. In Ref. [69], we compute the phase diagram for $\theta = 1.75°$, which yields sizable TR-symmetric insulating IVC regions, but none corresponding to CTIs. We also consider the inclusion of momentum-dependent tunneling in the single-particle continuum model, which captures the particle-hole asymmetry observed in the experimental phase diagram [64]. Again, we do not find any CTIs, suggesting that such states may not be robustly present in HTG.

F. Twisted transition metal dichalcogenide homobilayers

Twisted homobilayers of hexagonal TMDs such as $MoTe_2$ and WSe_2 are also ideal platforms for realizing narrow topological time-reversed bands. Unlike graphene-based systems, they have strong spin-orbit coupling such that the low-energy bands are spin-valley-locked to be either $K\uparrow$ or $K'\downarrow$ [72]. Twisted bilayer $MoTe_2$ ($t\text{MoTe}_2$) has attracted considerable attention because of its displacement field-tuned [100] Chern insulator at $\nu = -1$, and correlated topological phases, including fractional Chern insulators, at various other fillings [8–11,101].

We focus on $\theta = 3.4° - 4.0°$ $t\text{MoTe}_2$, where the lowest single-particle valence band has $C = +1$ (-1) in valley K (K') for small interlayer potentials ΔV as demonstrated with continuum model calculations [Fig. 10(a)]. This raises the question of whether a CTI_1 is feasible at $\nu = -1$. We note that the highest valence band is separated from the next valence band with opposite Chern number by $\lesssim 10$ meV, and there is a topological phase transition that trivializes the highest valence band at around $\Delta V = 26$ meV. As shown in Fig. 10(b), HF yields a valley-polarized Chern insulator at $\Delta V = 0$, while the ground state is a valley- and layer-polarized trivial insulator for strong interactions. For moderate interlayer potentials and weak/moderate interactions, we find a layer-polarized $\hat{\mathcal{T}}$-symmetric [102] IVC insulator [103]. However, this is not a CTI, as evidenced by the nonvanishing of IVC across the mBZ and the trivial valley-filtered Chern number of the unfilled HF band. While this is not surprising for large ΔV above the single-particle topological transition, the fact that this IVC state remains unfrustrated for smaller $\Delta V < 26$ meV implies

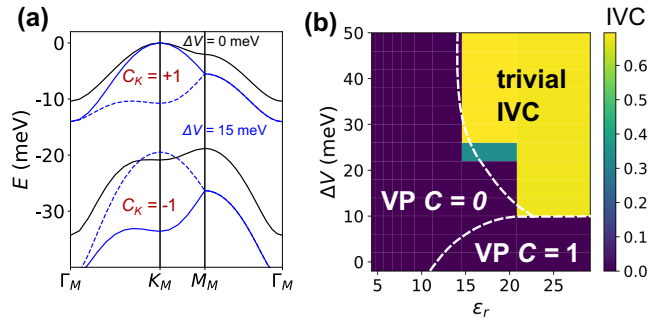


FIG. 10. Twisted bilayer $MoTe_2$ at $\theta = 4°$. (a) Single-particle valence band structure at $\Delta V = 0$ meV (black) and 15 meV (blue). Valley K (K') is shown with solid (dashed) lines. The band closest to charge neutrality has nontrivial valley Chern number for $\Delta V < 26$ meV. (b) Phase diagram calculated using 12×12 HF at $\nu = -1$. VP indicates fully valley polarized (which also implies spin polarized owing to spin-valley-locking). Trivial IVC denotes a $C = 0$ layer-polarized phase with no intervalley frustration. Similar results are obtained for $\theta = 3.4°, 3.7°$.

that interaction-induced hybridization with the next valence band removes the topological obstruction.

G. Twisted symmetric trilayer graphene

At the single-particle level, TSTG is $\hat{\mathcal{C}}_{2z}$ symmetric, and at zero or low interlayer potential, the HF ground states preserve this symmetry. However, at large interlayer potential, Ref. [29] found a spontaneously $\hat{\mathcal{C}}_{2z}$-breaking intervalley coherent state with nonzero intervalley boost vector $\boldsymbol{q}$, which is commensurate in the absence of strain. Figure 11 shows the phase diagram of unstrained TSTG at $\nu = 2$ in the displacement field-interaction plane, with the commensurate Kekulé spiral region now characterized as "trivial IVC", for reasons we now describe.

Characterizing possible intervalley frustration in the IVC phase is more nuanced in TSTG than in the other materials discussed so far. In the previous cases, for $\nu > 0$, there is only one empty band per spin sector that contains IVC (the higher

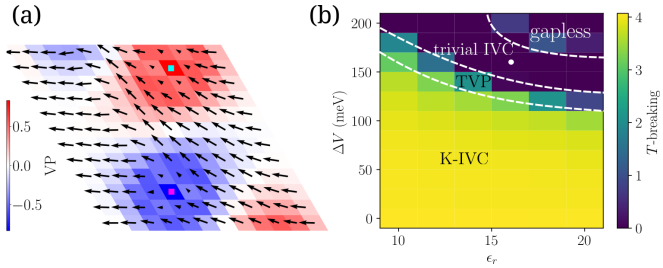


FIG. 11. Twisted symmetric trilayer graphene (TSTG) at $\theta = 1.56°$. (a) The order parameter of the IVC state at $\Delta V = 160$ meV and $\epsilon_r = 16$, from 12×12 HF. The extraction of the basis is explained in the text. No intervalley frustration is observed, as evidenced by lack of full valley polarization anywhere in the mBZ and zero winding of the order parameter around the mBZ. (b) Phase diagram from 12×12 HF at $\nu = 2$. TVP denoted tilted valley-polarized state. Besides the region labeled "gapless", the K-IVC region is also not gapped.

remote bands do not qualitatively affect the physics), and the valley-filtered basis is naturally extracted from this band. In TSTG, since the single-particle band structure has no spectral gaps, there is no clear distinction between central and remote bands, and at the interacting level, there are multiple bands per spin sector both above and below the Fermi energy, many of which are not isolated. This makes the identification of a suitable valley-filtered basis difficult. Nevertheless, we find the *first* band above Fermi energy to be isolated, at least for some parameters, from which we can extract a valley-filtered basis. The corresponding intervalley order parameter is shown in Fig. 11(a), which does not display winding of the IVC. As such, we conclude that the $\hat{\mathcal{C}}_{2z}$-breaking Kekulé spiral in TSTG is not a CTI.

IV. DISCUSSION

While we have investigated the HF phase diagrams for several moiré systems, as listed in Table I, the moiré paradigm offers near limitless combinations of constituent materials and tuning knobs that can generate favorable conditions for realizing textured excitonic states. So far, we have only uncovered CTIs in graphene-based platforms. Our calculations within a narrow twist angle range $\theta = 3.4° - 4.0°$ for twisted homobilayer $MoTe_2$ in Sec. III F have not yielded similar states. However, the single-particle models are known to vary significantly for different choices of TMDs and twist angles. For instance, for twisted bilayer WSe_2, as well as $t$$MoTe_2$ at smaller twist angles, density functional theory calculations have shown that the highest two valence moiré bands within a valley can have the same Chern numbers at zero displacement field [104]. This may influence the robustness of CTIs against trivialization of the intervalley coherence. Topological phases have also been experimentally observed in TMD heterobilayers [105]. Further exploration of the theoretical phase diagram is required to fully flesh out the nature of candidate IVC insulators in these TMD systems. Moiré platforms are natural potential hosts for CTIs because they often contain valleys that are mapped into each under time-reversal. More generally though, CTIs may arise as correlated insulators in other types of platforms if they are topological, are equipped with a time-reversal-odd $U(1)$ index, and exhibit competition between interactions and kinetic dispersion.

While we have found that several moiré materials favor the formation of CTIs in realistic parameter regimes, uncertainty in the modeling of the materials, in particular the effective interaction strength parameterized by ϵ_r, precludes more detailed predictions in the absence of specific experimental details. Other single-particle effects not treated here, such as strain (which is essential for the IKS, an example of an ETI in twisted bilayer and trilayer graphene [21]), would also impact the phase boundaries, including potentially widening the CTI regime. We also note that our calculations assume generalized translation symmetry on the moiré scale and hence ignores possible charge density wave (CDW) orders on this scale. Future work is required to establish the energetic competition of the CTI versus various moiré-scale density wave states.

CTIs are time-reversal invariant, meaning that, unlike Chern insulators, they do not produce a quantized charge Hall response, which makes their experimental detection more

challenging. In Ref. [57], the authors detected a $C = 0$ insulating state at $\nu = 1$ in TMBG at finite interlayer potential. Since valley-polarized states are expected to carry nonzero Chern numbers because of the noninteracting band topology, this provides an indirect piece of evidence for the existence of the CTI here. We note that the authors found nonvanishing anomalous Hall response at finite doping away from $\nu = 1$. An important direction therefore is to theoretically investigate whether time-reversal symmetry is broken when CTIs are doped away from integer fillings (as was studied in Ref. [106] for the IKS in TBG, which is an ETI). In cases where time-reversal continues to be preserved, then the CTI may be a potential correlated insulating parent state that can be doped to yield superconductivity, although this seems to occur very rarely in $\hat{C}_{2z}$-breaking moiré platforms.

Because of their finite intervalley coherence, CTIs in moiré systems are expected to produce translation symmetry-breaking patterns on the *atomic* scale, such as $\sqrt{3} \times \sqrt{3}$ Kekulé charge patterns observed with scanning tunneling microscopy in twisted graphene materials [27,28,107,108]. Detection of such patterns provides supporting evidence for the existence of IVC that is necessary for CTIs. Furthermore, the spiral wavevector $\boldsymbol{q}$ can be extracted from detailed analysis of the *moiré*-scale modulation of the IVC [27,28], which can be compared with theoretical predictions. We emphasize that, unlike the real-space IVC vortices detected in Ref. [27] *within* a moiré unit cell, the valley pseudospin texturing we have discussed for CTIs occurs in momentum space. As we have illustrated with an explicit example from TMBG, it is possible for a state without momentum space vortices (a "trivial IVC" insulator by our criteria) to still carry vortices in the real-space IVC-order parameter. Nevertheless, detailed real-space maps of the IVC texturing within a moiré cell can be fruitfully compared between experiment and theory to reinforce the interpretation of specific correlated states [27]. Finally, we propose that angle-resolved photoemission spectroscopy (ARPES) can potentially be used to directly detect the momentum-space texture of a CTI. ARPES allows the momentum-space structure of a material to be mapped out directly, and is sensitive to the valley-degree of freedom since electrons in the two valleys have different momenta. This allows the valley polarization pattern in momentum space to be mapped out [109]. In particular, the vortices where the state is fully valley polarized can be located, allowing the CTI order to be observed directly.

ACKNOWLEDGMENTS

We thank Jonah Herzog-Arbeitmann, Andrei Bernevig, and Jiabin Yu for useful discussions. This work was supported by a Leverhulme Trust International Professorship (Grant No. LIP-202-014, Z.W.), by a University of Zurich Postdoc Grant (FK-23-134, G.W.), by the European Research Council under the European Union Horizon 2020 Research and Innovation Programme via Grants Agreement No. 804213-TMCS (S.A.P.) and No. 101076597-SIESS (N.B.), and by EPSRC Grants EP/S020527/1 and EP/X030881/1 (S.H.S.). Y.H.K. is supported by a postdoctoral research fellowship at the Princeton Center for Theoretical Science.

DATA AVAILABILITY

The data are available upon reasonable request from the authors.

[1] Y. Cao, V. Fatemi, S. Fang, K. Watanabe, T. Taniguchi, E. Kaxiras, and P. Jarillo-Herrero, Unconventional superconductivity in magic-angle graphene superlattices, Nature (London) **556**, 43 (2018).

[2] M. Yankowitz, S. Chen, H. Polshyn, Y. Zhang, K. Watanabe, T. Taniguchi, D. Graf, A. F. Young, and C. R. Dean, Tuning superconductivity in twisted bilayer graphene, Science **363**, 1059 (2019).

[3] X. Lu, P. Stepanov, W. Yang, M. Xie, M. A. Aamir, I. Das, C. Urgell, K. Watanabe, T. Taniguchi, G. Zhang, A. Bachtold *et al.*, Superconductors, orbital magnets and correlated states in magic-angle bilayer graphene, Nature (London) **574**, 653 (2019).

[4] J. M. Park, Y. Cao, K. Watanabe, T. Taniguchi, and P. Jarillo-Herrero, Tunable strongly coupled superconductivity in magic-angle twisted trilayer graphene, Nature (London) **590**, 249 (2021).

[5] Y. Cao, V. Fatemi, A. Demir, S. Fang, S. L. Tomarken, J. Y. Luo, J. D. Sanchez-Yamagishi, K. Watanabe, T. Taniguchi, E. Kaxiras *et al.*, Correlated insulator behaviour at half-filling in magic-angle graphene superlattices, Nature (London) **556**, 80 (2018).

[6] A. L. Sharpe, E. J. Fox, A. W. Barnard, J. Finney, K. Watanabe, T. Taniguchi, M. A. Kastner, and D. Goldhaber-Gordon, Emergent ferromagnetism near three-quarters filling in twisted bilayer graphene, Science **365**, 605 (2019).

[7] M. Serlin, C. L. Tschirhart, H. Polshyn, Y. Zhang, J. Zhu, K. Watanabe, T. Taniguchi, L. Balents, and A. F. Young, Intrinsic quantized anomalous Hall effect in a moiré heterostructure, Science **367**, 900 (2020).

[8] H. Park, J. Cai, E. Anderson, Y. Zhang, J. Zhu, X. Liu, C. Wang, W. Holtzmann, C. Hu, Z. Liu *et al.*, Observation of fractionally quantized anomalous Hall effect, Nature (London) **622**, 74 (2023).

[9] J. Cai, E. Anderson, C. Wang, X. Zhang, X. Liu, W. Holtzmann, Y. Zhang, F. Fan, T. Taniguchi, K. Watanabe *et al.*, Signatures of fractional quantum anomalous Hall states in twisted $MoTe_2$, Nature (London) **622**, 63 (2023).

[10] Y. Zeng, Z. Xia, K. Kang, J. Zhu, P. Knüppel, C. Vaswani, K. Watanabe, T. Taniguchi, K. F. Mak, and J. Shan, Thermodynamic evidence of fractional Chern insulator in moiré $MoTe_2$, Nature (London) **622**, 69 (2023).

[11] F. Xu, Z. Sun, T. Jia, C. Liu, C. Xu, C. Li, Y. Gu, K. Watanabe, T. Taniguchi, B. Tong, J. Jia, Z. Shi, S. Jiang, Y. Zhang, X. Liu, and T. Li, Observation of integer and fractional quantum anomalous Hall effects in twisted bilayer $MoTe_2$, Phys. Rev. X **13**, 031037 (2023).

[12] Z. Lu, T. Han, Y. Yao, A. P. Reddy, J. Yang, J. Seo, K. Watanabe, T. Taniguchi, L. Fu, and L. Ju, Fractional quantum anomalous Hall effect in a graphene moire superlattice, Nature (London) **626**, 759 (2024).

[13] Y. Xie, A. T. Pierce, J. M. Park, D. E. Parker, E. Khalaf, P. Ledwith, Y. Cao, S. H. Lee, S. Chen, P. R. Forrester, K. Watanabe, T. Taniguchi, A. Vishwanath, P. Jarillo-Herrero, and A. Yacoby, Fractional Chern insulators in magic-angle twisted bilayer graphene, Nature (London) **600**, 439 (2021).

[14] A. Jaoui, I. Das, G. Di Battista, J. Díez-Mérida, X. Lu, K. Watanabe, T. Taniguchi, H. Ishizuka, L. Levitov, and D. K. Efetov, Quantum critical behaviour in magic-angle twisted bilayer graphene, Nat. Phys. **18**, 633 (2022).

[15] H. Polshyn, M. Yankowitz, S. Chen, Y. Zhang, K. Watanabe, T. Taniguchi, C. R. Dean, and A. F. Young, Large linear-in-temperature resistivity in twisted bilayer graphene, Nat. Phys. **15**, 1011 (2019).

[16] E. C. Regan, D. Wang, C. Jin, M. I. Bakti Utama, B. Gao, X. Wei, S. Zhao, W. Zhao, Z. Zhang, K. Yumigeta *et al.*, Mott and generalized Wigner crystal states in WSe_2/WS_2 moiré superlattices, Nature (London) **579**, 359 (2020).

[17] J. M. Park, Y. Cao, L. Xia, S. Sun, K. Watanabe, T. Taniguchi, and P. Jarillo-Herrero, Magic-angle multilayer graphene: A robust family of moiré superconductors, arXiv:2112.10760.

[18] Y. Zhang, R. Polski, C. Lewandowski, A. Thomson, Y. Peng, Y. Choi, H. Kim, K. Watanabe, T. Taniguchi, J. Alicea *et al.*, Promotion of superconductivity in magic-angle graphene multilayers, Science **377**, 1538 (2022).

[19] K. F. Mak and J. Shan, Semiconductor moirématerials, Nat. Nanotechnol. **17**, 686 (2022).

[20] S. L. Sondhi, A. Karlhede, S. A. Kivelson, and E. H. Rezayi, Skyrmions and the crossover from the integer to fractional quantum Hall effect at small Zeeman energies, Phys. Rev. B **47**, 16419 (1993).

[21] Y. H. Kwan, Z. Wang, G. Wagner, S. H. Simon, S. A. Parameswaran, and N. Bultinck, preceding paper, Textured exciton insulators, Phys. Rev. B **112**, 035129 (2025).

[22] N. Bultinck, S. Chatterjee, and M. P. Zaletel, Mechanism for anomalous Hall ferromagnetism in twisted bilayer graphene, Phys. Rev. Lett. **124**, 166601 (2020).

[23] A. Bouhon, A. M. Black-Schaffer, and R.-J. Slager, Wilson loop approach to fragile topology of split elementary band representations and topological crystalline insulators with time-reversal symmetry, Phys. Rev. B **100**, 195135 (2019).

[24] J. Ahn, S. Park, and B.-J. Yang, Failure of Nielsen-Ninomiya theorem and fragile topology in two-dimensional systems with space-time inversion symmetry: Application to twisted bilayer graphene at magic angle, Phys. Rev. X **9**, 021013 (2019).

[25] Z. Song, Z. Wang, W. Shi, G. Li, C. Fang, and B. A. Bernevig, All magic angles in twisted bilayer graphene are topological, Phys. Rev. Lett. **123**, 036401 (2019).

[26] Y. H. Kwan, G. Wagner, T. Soejima, M. P. Zaletel, S. H. Simon, S. A. Parameswaran, and N. Bultinck, Kekulé spiral order at all nonzero integer fillings in twisted bilayer graphene, Phys. Rev. X **11**, 041063 (2021).

[27] K. P. Nuckolls, R. L. Lee, M. Oh, D. Wong, T. Soejima, J. P. Hong, D. Călugăru, J. Herzog-Arbeitman, B. A. Bernevig, K. Watanabe *et al.*, Quantum textures of the many-body wavefunctions in magic-angle graphene, Nature (London) **620**, 525 (2023).

[28] H. Kim, Y. Choi, É. Lantagne-Hurtubise, C. Lewandowski, A. Thomson, L. Kong, H. Zhou, E. Baum, Y. Zhang, L. Holleis *et al.*, Imaging inter-valley coherent order in magic-angle twisted trilayer graphene, Nature (London) **623**, 942 (2023).

[29] Z. Wang, Y. H. Kwan, G. Wagner, N. Bultinck, S. H. Simon, and S. A. Parameswaran, Kekulé spirals and charge transfer cascades in twisted symmetric trilayer graphene, Phys. Rev. B **109**, L201119 (2024).

[30] C. Zhang, T. Zhu, S. Kahn, S. Li, B. Yang, C. Herbig, X. Wu, H. Li, K. Watanabe, T. Taniguchi *et al.*, Visualizing delocalized correlated electronic states in twisted double bilayer graphene, Nat. Commun. **12**, 2516 (2021).

[31] C. Rubio-Verdú, S. Turkel, Y. Song, L. Klebl, R. Samajdar, M. S. Scheurer, J. W. F. Venderbos, K. Watanabe, T. Taniguchi, H. Ochoa *et al.*, Moiré nematic phase in twisted double bilayer graphene, Nat. Phys. **18**, 196 (2022).

[32] S.-y. Li, Z. Wang, Y. Xue, Y. Wang, S. Zhang, J. Liu, Z. Zhu, K. Watanabe, T. Taniguchi, H.-j. Gao *et al.*, Imaging topological and correlated insulating states in twisted monolayer-bilayer graphene, Nat. Commun. **13**, 4225 (2022).

[33] This should be contrasted against the ETI setting, where single-valley $\hat{\mathcal{C}}_{2z}\hat{\mathcal{T}}$ symmetry is essential [21].

[34] Y.-H. Zhang, D. Mao, and T. Senthil, Twisted bilayer graphene aligned with hexagonal boron nitride: Anomalous Hall effect and a lattice model, Phys. Rev. Res. **1**, 033126 (2019).

[35] Y.-H. Zhang, D. Mao, Y. Cao, P. Jarillo-Herrero, and T. Senthil, Nearly flat Chern bands in moiré superlattices, Phys. Rev. B **99**, 075127 (2019).

[36] R. Bistritzer and A. H. MacDonald, Moiré bands in twisted double-layer graphene, Proc. Natl. Acad. Sci. USA **108**, 12233 (2011).

[37] G. W. Burg, J. Zhu, T. Taniguchi, K. Watanabe, A. H. MacDonald, and E. Tutuc, Correlated insulating states in twisted double bilayer graphene, Phys. Rev. Lett. **123**, 197702 (2019).

[38] Y. Cao, D. Rodan-Legrain, O. Rubies-Bigorda, J. M. Park, K. Watanabe, T. Taniguchi, and P. Jarillo-Herrero, Tunable correlated states and spin-polarized phases in twisted bilayer–bilayer graphene, Nature (London) **583**, 215 (2020).

[39] R. Du, J. Xiao, D. Zhang, X. Cai, S. Jiang, F. Lian, K. Watanabe, T. Taniguchi, L. Wang, and G. Yu, Ferroelectricity in twisted double bilayer graphene, 2D Mater. **11**, 025015 (2024).

[40] M. He, Y. Li, J. Cai, Y. Liu, K. Watanabe, T. Taniguchi, X. Xu, and M. Yankowitz, Symmetry breaking in twisted double bilayer graphene, Nat. Phys. **17**, 26 (2021).

[41] L. Liu, S. Zhang, Y. Chu, C. Shen, Y. Huang, Y. Yuan, J. Tian, J. Tang, Y. Ji, R. Yang *et al.*, Isospin competitions and valley polarized correlated insulators in twisted double bilayer graphene, Nat. Commun. **13**, 3292 (2022).

[42] X. Liu, Z. Hao, E. Khalaf, J. Y. Lee, Y. Ronen, H. Yoo, D. Haei Najafabadi, K. Watanabe, T. Taniguchi, A. Vishwanath, and P. Kim, Tunable spin-polarized correlated states in twisted double bilayer graphene, Nature (London) **583**, 221 (2020).

[43] P. Rickhaus, F. K. de Vries, J. Zhu, E. Portoles, G. Zheng, M. Masseroni, A. Kurzmann, T. Taniguchi, K. Watanabe, A. H. MacDonald *et al.*, Correlated electron-hole state in twisted double-bilayer graphene, Science **373**, 1257 (2021).

[44] C. Shen, Y. Chu, Q. Wu, N. Li, S. Wang, Y. Zhao, J. Tang, J. Liu, J. Tian, K. Watanabe *et al.*, Correlated states in twisted double bilayer graphene, Nat. Phys. **16**, 520 (2020).

[45] Y. Zhu, Y. Chen, Q. Li, Y. Chen, Y. Huang, W. Zhu, D. An, J. Song, Q. Gan, K. Wang *et al.*, Tunable multi-bands in twisted double bilayer graphene, 2D Mater. **9**, 034001 (2022).

[46] M. He, J. Cai, Y.-H. Zhang, Y. Liu, Y. Li, T. Taniguchi, K. Watanabe, D. H. Cobden, M. Yankowitz, and X. Xu, Symmetry-broken Chern insulators in twisted double bilayer graphene, Nano Lett. **23**, 11066 (2023).

[47] M. Koshino, Band structure and topological properties of twisted double bilayer graphene, Phys. Rev. B **99**, 235406 (2019).

[48] J. Liu, Z. Ma, J. Gao, and X. Dai, Quantum valley Hall effect, orbital magnetism, and anomalous Hall effect in twisted multilayer graphene systems, Phys. Rev. X **9**, 031021 (2019).

[49] N. R. Chebrolu, B. L. Chittari, and J. Jung, Flat bands in twisted double bilayer graphene, Phys. Rev. B **99**, 235417 (2019).

[50] J. Y. Lee, E. Khalaf, S. Liu, X. Liu, Z. Hao, P. Kim, and A. Vishwanath, Theory of correlated insulating behaviour and spin-triplet superconductivity in twisted double bilayer graphene, Nat. Commun. **10**, 5333 (2019).

[51] F. Haddadi, Q. Wu, A. J. Kruchkov, and O. V. Yazyev, Moiré flat bands in twisted double bilayer graphene, Nano Lett. **20**, 2410 (2020).

[52] For all materials considered, we model the displacement field by a linearly varying potential that differs by ΔV between the outermost layers.

[53] J. Jung and A. H. MacDonald, Accurate tight-binding models for the π bands of bilayer graphene, Phys. Rev. B **89**, 035405 (2014).

[54] N. N. T. Nam and M. Koshino, Lattice relaxation and energy band modulation in twisted bilayer graphene, Phys. Rev. B **96**, 075311 (2017).

[55] S. Carr, S. Fang, Z. Zhu, and E. Kaxiras, Exact continuum model for low-energy electronic states of twisted bilayer graphene, Phys. Rev. Res. **1**, 013001 (2019).

[56] S. Chen, M. He, Y.-H. Zhang, V. Hsieh, Z. Fei, K. Watanabe, T. Taniguchi, D. H. Cobden, X. Xu, C. R. Dean, and M. Yankowitz, Electrically tunable correlated and topological states in twisted monolayer–bilayer graphene, Nat. Phys. **17**, 374 (2021).

[57] M. He, Y.-H. Zhang, Y. Li, Z. Fei, K. Watanabe, T. Taniguchi, X. Xu, and M. Yankowitz, Competing correlated states and abundant orbital magnetism in twisted monolayer-bilayer graphene, Nat. Commun. **12**, 4727 (2021).

[58] H. Polshyn, J. Zhu, M. A. Kumar, Y. Zhang, F. Yang, C. L. Tschirhart, M. Serlin, K. Watanabe, T. Taniguchi, A. H. MacDonald, and A. F. Young, Electrical switching of magnetic order in an orbital Chern insulator, Nature (London) **588**, 66 (2020).

[59] H. Polshyn, Y. Zhang, M. A. Kumar, T. Soejima, P. Ledwith, K. Watanabe, T. Taniguchi, A. Vishwanath, M. P. Zaletel, and A. F. Young, Topological charge density waves at half-integer filling of a moiré superlattice, Nat. Phys. **18**, 42 (2022).

[60] S. Xu, M. M. Al Ezzi, N. Balakrishnan, A. Garcia-Ruiz, B. Tsim, C. Mullan, J. Barrier, N. Xin, B. A. Piot, T. Taniguchi *et al.*, Tunable van Hove singularities and correlated states in twisted monolayer–bilayer graphene, Nat. Phys. **17**, 619 (2021).

[61] C. Zhang, T. Zhu, T. Soejima, S. Kahn, K. Watanabe, T. Taniguchi, A. Zettl, F. Wang, M. P. Zaletel, and M. F. Crommie, Local spectroscopy of a gate-switchable moiré quantum anomalous Hall insulator, Nat. Commun. **14**, 3595 (2023).

[62] P. J. Ledwith, A. Vishwanath, and E. Khalaf, Family of ideal Chern flatbands with arbitrary Chern number in chiral twisted graphene multilayers, Phys. Rev. Lett. **128**, 176404 (2022).

[63] R. Su, D. Waters, B. Zhou, K. Watanabe, T. Taniguchi, Y.-H. Zhang, M. Yankowitz, and J. Folk, Moiré-driven topological electronic crystals in twisted graphene, Nature (London) **637**, 1084 (2025).

[64] L.-Q. Xia, S. C. de la Barrera, A. Uri, A. Sharpe, Y. H. Kwan, Z. Zhu, K. Watanabe, T. Taniguchi, D. Goldhaber-Gordon, L. Fu, T. Devakul, and P. Jarillo-Herrero, Topological bands and correlated states in helical trilayer graphene, Nat. Phys. **21**, 239 (2025).

[65] T. Devakul, P. J. Ledwith, L.-Q. Xia, A. Uri, S. C. de la Barrera, P. Jarillo-Herrero, and L. Fu, Magic-angle helical trilayer graphene, Sci. Adv. **9**, eadi6063 (2023).

[66] N. Nakatsuji, T. Kawakami, and M. Koshino, Multiscale lattice relaxation in general twisted trilayer graphenes, Phys. Rev. X **13**, 041007 (2023).

[67] Y. H. Kwan, P. J. Ledwith, C. F. B. Lo, and T. Devakul, Strong-coupling topological states and phase transitions in helical trilayer graphene, Phys. Rev. B **109**, 125141 (2024).

[68] The interlayer tunneling here does not include effects of the momentum dependence of the tunneling [64]. See Ref. [69] for a discussion of this correction.

[69] See Supplemental Material at http://link.aps.org/supplemental/10.1103/chsd-123t for numerical results with the "graphene" subtraction scheme, gauge fixing, and other additional results.

[70] J. Yu, J. Herzog-Arbeitman, M. Wang, O. Vafek, B. A. Bernevig, and N. Regnault, Fractional Chern insulators versus nonmagnetic states in twisted bilayer $MoTe_2$, Phys. Rev. B **109**, 045147 (2024).

[71] Y. Jia, J. Yu, J. Liu, J. Herzog-Arbeitman, Z. Qi, H. Pi, N. Regnault, H. Weng, B. A. Bernevig, and Q. Wu, Moiré fractional Chern insulators. I. First-principles calculations and continuum models of twisted bilayer $MoTe_2$, Phys. Rev. B **109**, 205121 (2024).

[72] F. Wu, T. Lovorn, E. Tutuc, I. Martin, and A. H. MacDonald, Topological insulators in twisted transition metal dichalcogenide homobilayers, Phys. Rev. Lett. **122**, 086402 (2019).

[73] C. Wang, X.-W. Zhang, X. Liu, Y. He, X. Xu, Y. Ran, T. Cao, and D. Xiao, Fractional Chern insulator in twisted bilayer $MoTe_2$, Phys. Rev. Lett. **132**, 036501 (2024).

[74] A. P. Reddy, F. Alsallom, Y. Zhang, T. Devakul, and L. Fu, Fractional quantum anomalous Hall states in twisted bilayer $MoTe_2$ and WSe_2, Phys. Rev. B **108**, 085117 (2023).

[75] Y. Cao, J. M. Park, K. Watanabe, T. Taniguchi, and P. Jarillo-Herrero, Pauli-limit violation and re-entrant superconductivity in moiré graphene, Nature (London) **595**, 526 (2021).

[76] Z. Hao, A. M. Zimmerman, P. Ledwith, E. Khalaf, D. H. Najafabadi, K. Watanabe, T. Taniguchi, A. Vishwanath, and P. Kim, Electric field–tunable superconductivity in alternating-

twist magic-angle trilayer graphene, Science **371**, 1133 (2021).

[77] H. Kim, Y. Choi, C. Lewandowski, A. Thomson, Y. Zhang, R. Polski, K. Watanabe, T. Taniguchi, J. Alicea, and S. Nadj-Perge, Evidence for unconventional superconductivity in twisted trilayer graphene, Nature (London) **606**, 494 (2022).

[78] Y. Li, S. Zhang, F. Chen, L. Wei, Z. Zhang, H. Xiao, H. Gao, M. Chen, S. Liang, D. Pei, L. Xu *et al.*, Observation of coexisting Dirac bands and moiré flat bands in magic-angle twisted trilayer graphene, Adv. Mater. **34**, 2205996 (2022).

[79] J.-X. Lin, P. Siriviboon, H. D. Scammell, S. Liu, D. Rhodes, K. Watanabe, T. Taniguchi, J. Hone, M. S. Scheurer, and J. I. A. Li, Zero-field superconducting diode effect in small-twist-angle trilayer graphene, Nat. Phys. **18**, 1221 (2022).

[80] X. Liu, N. J. Zhang, K. Watanabe, T. Taniguchi, and J. I. A. Li, Isospin order in superconducting magic-angle twisted trilayer graphene, Nat. Phys. **18**, 522 (2022).

[81] C. Shen, P. J. Ledwith, K. Watanabe, T. Taniguchi, E. Khalaf, A. Vishwanath, and D. K. Efetov, Dirac spectroscopy of strongly correlated phases in twisted trilayer graphene, Nat. Mater. **22**, 316 (2023).

[82] S. Turkel, J. Swann, Z. Zhu, M. Christos, K. Watanabe, T. Taniguchi, S. Sachdev, M. S. Scheurer, E. Kaxiras, C. R. Dean, and A. N. Pasupathy, Orderly disorder in magic-angle twisted trilayer graphene, Science **376**, 193 (2022).

[83] S.-J. Yang, J.-H. Jung, E. Lee, E. Han, M.-Y. Choi, D. Jung, S. Choi, J.-H. Park, D. Oh, S. Noh *et al.*, Wafer-scale programmed assembly of one-atom-thick crystals, Nano Lett. **22**, 1518 (2022).

[84] N. J. Zhang, J.-X. Lin, D. V. Chichinadze, Y. Wang, K. Watanabe, T. Taniguchi, L. Fu, and J. I. A. Li, Angle-resolved transport non-reciprocity and spontaneous symmetry breaking in twisted trilayer graphene, Nat. Mater. **23**, 356 (2024).

[85] X. Li, F. Wu, and A. H. MacDonald, Electronic structure of single-twist trilayer graphene, arXiv:1907.12338.

[86] E. Khalaf, A. J. Kruchkov, G. Tarnopolsky, and A. Vishwanath, Magic angle hierarchy in twisted graphene multilayers, Phys. Rev. B **100**, 085109 (2019).

[87] D. Calugaru, F. Xie, Z.-D. Song, B. Lian, N. Regnault, and B. A. Bernevig, Twisted symmetric trilayer graphene: Single-particle and many-body Hamiltonians and hidden nonlocal symmetries of trilayer moiré systems with and without displacement field, Phys. Rev. B **103**, 195411 (2021).

[88] M. Xie and A. H. MacDonald, Nature of the correlated insulator states in twisted bilayer graphene, Phys. Rev. Lett. **124**, 097601 (2020).

[89] J. Kang and O. Vafek, Strong coupling phases of partially filled twisted bilayer graphene narrow bands, Phys. Rev. Lett. **122**, 246401 (2019).

[90] N. Bultinck, E. Khalaf, S. Liu, S. Chatterjee, A. Vishwanath, and M. P. Zaletel, Ground state and hidden symmetry of magic-angle graphene at even integer filling, Phys. Rev. X **10**, 031034 (2020).

[91] B. Lian, Z.-D. Song, N. Regnault, D. K. Efetov, A. Yazdani, and B. A. Bernevig, Twisted bilayer graphene. IV. Exact insulator ground states and phase diagram, Phys. Rev. B **103**, 205414 (2021).

[92] T. Wang, D. E. Parker, T. Soejima, J. Hauschild, S. Anand, N. Bultinck, and M. P. Zaletel, Ground-state order in magic-angle graphene at filling $\nu=-3$: A full-scale density matrix renormalization group study, Phys. Rev. B **108**, 235128 (2023).

[93] Reference [69] details how we implement a smooth but nonperiodic gauge fixing.

[94] We briefly discuss the situation where multiple HF bands are proximate in energy in Sec. III G.

[95] The hole order parameter would differ by a minus sign.

[96] Within spin-collinear HF calculations, states with different IVC angles in the two spin sectors are degenerate with $SU(2)_s$-symmetric IVC states.

[97] C. Fang, M. J. Gilbert, and B. A. Bernevig, Bulk topological invariants in noninteracting point group symmetric insulators, Phys. Rev. B **86**, 115112 (2012).

[98] Y. H. Kwan, Z. Wang, G. Wagner, S. H. Simon, S. A. Parameswaran, and N. Bultinck (unpublished).

[99] D. Guerci, Y. Mao, and C. Mora, Chern mosaic and ideal flat bands in equal-twist trilayer graphene, Phys. Rev. Res. **6**, L022025 (2024).

[100] E. Anderson, F.-R. Fan, J. Cai, W. Holtzmann, T. Taniguchi, K. Watanabe, D. Xiao, W. Yao, and X. Xu, Programming correlated magnetic states with gate-controlled moiré geometry, Science **381**, 325 (2023).

[101] K. Kang, B. Shen, Y. Qiu, K. Watanabe, T. Taniguchi, J. Shan, and K. F. Mak, Observation of the fractional quantum spin Hall effect in moiré $MoTe_2$, Nature (London) **628**, 522 (2024).

[102] Our definition of $\hat{\mathcal{T}}$ for this subsection interchanges $(K\uparrow) \leftrightarrow (K'\downarrow)$ and satisfies $\hat{\mathcal{T}}^2 = 1$.

[103] T. Wang, T. Devakul, M. P. Zaletel, and L. Fu, Topological magnets and magnons in twisted bilayer $MoTe_2$ and WSe_2, arXiv:2306.02501.

[104] X.-W. Zhang, C. Wang, X. Liu, Y. Fan, T. Cao, and D. Xiao, Polarization-driven band topology evolution in twisted $MoTe_2$ and WSe_2, Nat. Commun. **15**, 4223 (2024).

[105] T. Li, S. Jiang, B. Shen, Y. Zhang, L. Li, Z. Tao, T. Devakul, K. Watanabe, T. Taniguchi, L. Fu *et al.*, Quantum anomalous Hall effect from intertwined moiré bands, Nature (London) **600**, 641 (2021).

[106] G. Wagner, Y. H. Kwan, N. Bultinck, S. H. Simon, and S. A. Parameswaran, Global phase diagram of the normal state of twisted bilayer graphene, Phys. Rev. Lett. **128**, 156401 (2022).

[107] D. Calugaru, N. Regnault, M. Oh, K. P. Nuckolls, D. Wong, R. L. Lee, A. Yazdani, O. Vafek, and B. A. Bernevig, Spectroscopy of twisted bilayer graphene correlated insulators, Phys. Rev. Lett. **129**, 117602 (2022).

[108] J. P. Hong, T. Soejima, and M. P. Zaletel, Detecting symmetry breaking in magic angle graphene using scanning tunneling microscopy, Phys. Rev. Lett. **129**, 147001 (2022).

[109] If the underlying Chern bands instead arise from opposite spin projections, then spin-resolved ARPES would be able to detect the spin polarization pattern.